JILA, CU Boulder/NIST
ETH Zurich, Department of Physics

MASTER'S THESIS

TOWARDS A DEGENERATE FERMI GAS OF STRONTIUM-87 IN A 3D OPTICAL LATTICE

by Nelson Darkwah Oppong

December 2015

Under the supervision of

Prof. Dr. Jun Ye
JILA
CU Boulder/NIST, USA

Prof. Dr. Jonathan Home
Institute for Quantum Electronics
ETH Zurich, Switzerland

ABSTRACT

We have designed and constructed a new apparatus towards evaporatively cooling strontium-87 in a far off-resonant optical dipole trap. The theory of far off-resonant optical traps is explained and we derive equations for heating in optical dipole traps due to intensity and pointing noise. A high power laser setup for 1064 nm light delivers a total power of up to 20 W for trapping and evaporatively cooling strontium-87. The 1064 nm light is delivered with photonic crystal fibers, reaching up to 18 W through a single optical fiber using a water-cooled high-power fiber connector. We present a design of a low noise photodetector that is used in an intensity servo for the 1064 nm laser system to suppress intensity noise by up to 40 dB. Preliminary results from the first attempts of evaporatively cooling strontium-87 atoms in a crossed optical dipole trap yield a $T/T_F = 0.5$ per spin state assuming a uniform distribution across all ten nuclear spin states.

Submitted: December 8, 2015
Version: May 25, 2016

Please note that this is *not* the original version. Changes have been made to fix a few typos. However, the content is entirely unchanged. Please send an email to the author at nelsond@phys.ethz.ch to receive the original version.

Git commit `357476c01dd51c0f904bd29c1d99ba7a40efc306`

ACKNOWLEDGMENTS

The last six months have been an exciting and fun experience. I have been very fortunate to have the chance to work with Jun and his group. The people from Jun's group all share exceptional technical skills and a deep understanding of physics. Jun is not only a brilliant PI but also a truly kind person. He always takes time for his students and I was fortunate to learn a lot of things from him. I am still fascinated by the intuition he has for technical challenges of experiments.

I would also like to thank Jonathan Home, my adviser at ETH, who supported my application to Jun's group and kindly agreed to supervise and grade my thesis.

Everyone in Jun's group was extremely kind to me. I really appreciate the time people took to explain physics to me. A special thanks goes to the strontium-2 gang: Sara Campbell, Ross Hutson, Edward Marti, and Akihisa Goban. They not only shared my appreciation for good beer but also taught me numerous things about precision measurements, cold atoms, and science in general. Working with them has been great fun and I will miss them. I not only enjoyed lunch and dinner with people from strontium-1 (Sarah Bromley, Xibo Zhang, Tobias Bothwell, Shimon Kolkowitz, and John Robinson) and stable lasers (Wei Zhang and Lindsay Sonderhouse) but also had the chance to learn from them during many interesting discussions about physics and other topics. I would like to thank Craig Benko from whom I have learned a lot about high power optics and whose recommendations made the setup of the 1064 nm laser system less painful. Thanks also to Bryce Bjork who kindly helped me with thermal imaging and monitoring of the high power fiber connectors. The staff from the instrument and electronics shop has helped me with numerous projects and I am thankful for their time and hard work. I gratefully acknowledge financial support from the *Studienstiftung des deutschen Volkes* (German National Academic Foundation) for my Master's thesis project in Jun's group. I thank my family for their continuous support and Sarah Klewes for her understanding and great patience.

We thank Dylan Cotta and Prof. Stephan Kuhr for their generous help with using photonic crystal fibers for high-power laser light.

CONTENTS

LIST OF FIGURES

LIST OF TABLES

LIST OF ABBREVIATIONS

ac Alternating current

AOM Acousto-optical modulator

AR Anti-reflective

CNC Computer numerical control

dc Direct current

ECDL External-cavity diode lasers

FET Field-effect transistor

FFT Fast Fourier transform

FIFO First in first out

FORT Far off-resonant trap

GBP Gain-bandwidth product

GUI Graphical user interface

HR High-reflection

HWP Half-wave plate

InGaAs Indium gallium arsenide

NA Numerical aperture

Nd:YAG Neodymium-doped yttrium aluminium garnet

NIR Near-infrared

PBS Polarizing beam spliter

PCB Printed circuit board

PID Proportional-integral-derivative

PSD Power spectral density

QWP Quarter-wave plate

RF Radio frequency

SBS Stimulated Brillouin scattering

Si Silicon

SNR Signal-to-noise ratio

TIA Transimpedance amplifier

UHV Ultra high vacuum

1

INTRODUCTION

1.1 GENERAL CONTEXT

Previous efforts of the Strontium-2 experiment at Ye Labs/JILA were focused on highly precise and accurate clock measurements. Fermionic strontium-87 was cooled and loaded into a 1D magic wavelength[1] optical lattice to measure the narrow $^1S_0 \rightarrow {}^3P_0$ transition [1]. The required stability of the clock laser at 698 nm is achieved by locking an external-cavity diode laser (ECDL) to a 40 cm cavity with a stability of 10^{-16} at 1 s [2]. Future efforts are to continue the improvement of a clock with a low-entropy quantum gas, which will also help with the investigation of quantum many-body physics. Fermions in optical lattices at low temperature allow us to simulate solid state Hamiltonians, realize novel quantum phases, and study their transitions. For example, the high spectroscopic resolution given by the clock laser might allow observations of novel magnetic phases given rise to by the (large) SU(N) symmetry of the ground state of strontium-87 [3].

The complete experiment - including the UHV chamber – has been rebuilt and three major technical changes are introduced:

(i) A new UHV chamber with more vacuum pumps is used to achieve a pressure of 10^{-11} Torr compared to 10^{-10} Torr in the old experiment.

(ii) An optical dipole trap with a wavelength of 1064 nm is used to evaporatively cool the atoms and to achieve a low-entropy gas prior to loading into the 3D optical lattice.

(iii) A new laser system is used for the optical lattice. The new 813 nm laser system delivers more power at 813 nm, which is required for the 3D optical lattice.

[1] At the magic wavelength, an optical dipole trap will create identical potentials for the ground and excited states. A superposition state, as is used in a clock, will remain coherent for an extended time in a magic wavelength trap.

The author was mainly involved in (ii) and (iii). The work on (ii) is completed but the laser system for the optical lattice (iii) is not completed yet. The complete outline of this thesis is given in the next section.

1.2 THESIS OUTLINE

This thesis gives an overview of the experiment, discusses some technical changes on the rebuild of the experiment and explains the basic theoretical frameworks. The thesis is structured into four chapters excluding the introductory chapter. The second chapter introduces the theoretical background for optical trapping in running and standing wave configurations. Rate equations for heating in optical dipole traps are derived and evaluated in this chapter as well. The third chapter explains the experimental apparatus and discusses technical aspects of the 1064 nm laser setup, including high-power photonic crystal fibers. The fourth chapter explains the main experimental techniques employed for optical trapping. In this chapter, the design of the photodetectors and intensity servo are explained in detail. The fifth and last chapter explains the experimental sequence, presents a few early experimental results and summarizes the overall findings of this thesis. Schematics and PCB designs as well as source code can be found in the appendices.

2

THEORY OF OPTICAL TRAPPING

Remarkably, trapping particles by an off-resonant optical/electric fields was first proposed by the Soviet-Armenian physicist Askaryan in 1962 – long before laser cooling was invented [4]. We use far-off resonant traps to capture atoms from the magneto-optical trap, evaporatively cool them towards quantum degeneracy, and load the degenerate atoms into an optical lattice. This chapter establishes the basic theoretical background for far-off resonant traps and heating in those traps. This is crucial to understand the experimental techniques explained in the next chapter. We also briefly discuss ultra-cold fermions in harmonic potentials at the end of this chapter.

2.1 FAR OFF-RESONANT TRAPS

Far off-resonant traps (FORTs) are optical traps where the frequency of the light is far detuned from any atomic resonances. The detuning $\Delta = \omega - \omega_0$ is defined as the difference between the frequency of the driving electric field (ω) and the frequency of the atomic resonance (ω_0). The advantages of FORTs are that many different atomic species can be trapped with the same wave length and scattering is reduced, which increases the lifetime of atoms in the trap. We give a short introduction into the physics of FORTs and discuss running and standing wave trap geometries in this section.

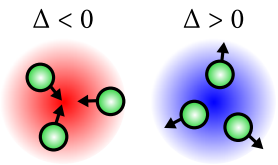

FIGURE 2.1: Illustration of optical dipole potentials for negative (red) and positive (blue) detunings. The red-detuned potential attracts atoms into the bright center and the blue-detuned potential pushes the atoms out of the bright into the dark center.

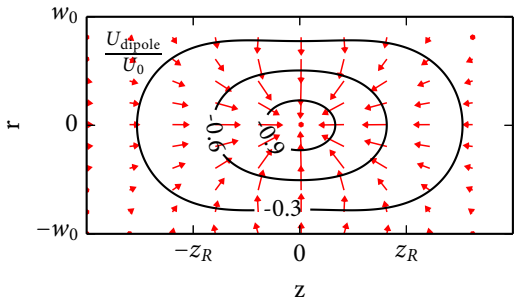

FIGURE 2.2: Example plot of the force (red arrows) in an optical dipole trap formed by running Gaussian beam. The normalized potential depth is shown as a contour plot (black). Length is defined in terms of the $1/e^2$ beam radius w_0 and the Rayleigh length z_R.

If an atom is placed into laser light, with an ac electric field $\vec{E}$, an atomic dipole moment $\vec{p}$ is induced. The interaction potential U_{dipole} of the $\vec{E}$ field and the atom is given as [5]

$$U_{\text{dipole}}(\vec{r}) = -\frac{1}{2}\langle \vec{p} \cdot \vec{E}(\vec{r})\rangle = -\frac{1}{2\epsilon_0 c}\text{Re}(\alpha)\vec{I}(\vec{r}). \tag{2.1}$$

Here α is the atomic polarizability defined as $|\vec{p}| = \alpha|\vec{E}|$, and $\vec{I} = I \cdot \hat{E}$ with $|\vec{I}| = |E|^2$ is the intensity of the driving electric field of the laser multiplied with the unit vector of the electric field $\vec{E}$. This potential generates the dipole force $\vec{F}_{\text{dipole}}$ with [5]

$$F_{\text{dipole}}(\vec{r}) = -\nabla U_{\text{dipole}}(\vec{r}) = \frac{1}{2\epsilon_0 c}\text{Re}(\alpha)\nabla\vec{I}. \tag{2.2}$$

An example optical potential and the resulting force is shown in Figure 2.2. We directly find that for $\text{Re}(\alpha) > 0$ the atoms are pushed towards maximum intensity and for $\text{Re}(\alpha) < 0$ atoms are pushed towards minimum intensity. Furthermore, the imaginary part of the polarizability yields the scattering rate as a function of position $\vec{r}$ [5]

$$\Gamma_{\text{scattering}}(\vec{r}) = \frac{1}{\hbar\epsilon_0 c}\text{Im}(\alpha)I(\vec{r}). \tag{2.3}$$

Here $I(\vec{r})$ is the intensity as a function of position. The scattering rate is the rate at which photons from the driving field are elastically scattered. For a two-level atom in the rotating wave approximation (i.e. the detuning from the resonance is small compared to the resonance frequency) we find the dipole potential U_{dipole} and the scattering rate $\Gamma_{\text{scattering}}$ to be [5]:

$$U_{\text{dipole}}(\vec{r}) = \frac{3\pi c^2}{2\omega_0^3}\frac{\Gamma}{\Delta}I(\vec{r}) \tag{2.4}$$

$$\Gamma_{\text{scattering}}(\vec{r}) = \frac{3\pi c^2}{2\hbar\omega_0^3}\left(\frac{\Gamma}{\Delta}\right)^2 I(\vec{r}) \tag{2.5}$$

Here, Γ is the decay rate from the excited state to the ground state defined in terms of the dipole matrix element. Thus, atoms can be trapped at a maximum of red-detuned light ($\Delta < 0$) and at a minimum of blue-detuned light ($\Delta > 0$). In a multi-level atom the expression for the atomic polarizability is more complicated and depends on all levels accessible from the ground state. Furthermore, we find that the polarizability depends on the spin state of the atom and polarization of the light, leading to vector and tensor polarizabilitiy in addition to the scalar term derived above. However, even neglecting polarization and using only the scalar theory in a two level atom, we find these important results:

- The potential depth is directly proportional to the intensity $I(\vec{r})$ for a fixed atomic state and wavelength of the driving laser field. Therefore we can limit the discussion of trap geometries in the next section to intensity distributions.
- Red-detuned light traps the atoms in maximum intensity and blue detuned light traps the atoms in minimum intensity. Thus, atoms experience an ac Stark shift in a red-detuned trap because the trapping potential has the minimum at maximum intensity.
- The potential depth scales with $1/\Delta$ but the scattering scales with $1/\Delta^2$. Thus, it is favorable to choose a large detuning and power to minimize scattering while preserving the conservative dipole force for trapping.

The optical dipole trap at 1064 nm and the optical lattice at 813 nm used in our experiment are both relatively far red detuned from atomic resonances (compared to the strong transitions at 461nm (for the ground state) and 679nm (for the $^3P_0$ excited state). Note that the choice of the laser wavelength for our optical dipole trap is based on the commercial availability of low-noise high power lasers. Lasers at 1064 nm find applications such as medicine and laser cutting and high power single-mode lasers ($\approx$ 50 W) are readily available.

2.2 OPTICAL DIPOLE TRAP GEOMETRIES

We generate the trapping potential at the high intensity peak using focused laser beams, which are well described by Gaussian beams. First, we discuss the running wave configuration and the harmonic approximation. Second, the standing wave configuration and the periodic harmonic approximation are explained. The actual trap configuration for the running wave optical dipole trap in the experiment can be found in Section 5.3.

The electric field of a Gaussian beam as a function of transverse distance r and

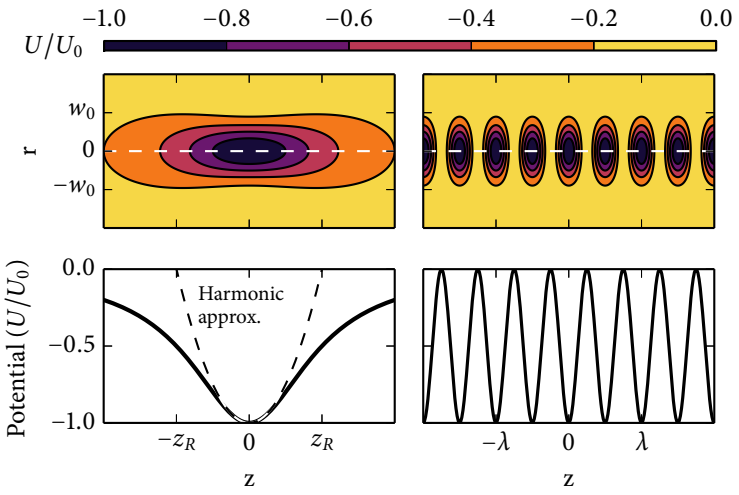

FIGURE 2.3: Running wave (left) and standing wave (right) normalized optical trap geometries for $\lambda = 1064\,\text{nm}$ and $w_0 = 100\,\mu\text{m}$. Length is given in units of the $1/e^2$ beam radius w_0 and the Rayleigh length z_R for the running wave, and in units of w_0 and the watvelength λ for the standing wave. The contour plots of the 2D potentials are shown in the top row. The white dashed lines indicate the plane for which 1D plots are shown in the bottom row.

longitudinal distance z is given as [6, p. 77]

$$E(r,z) = E_0 \frac{w_0}{w(z)} \exp\left\{ i\zeta(z) - \frac{r^2}{w^2(z)} - ikz - ik\frac{r^2}{2R(z)} \right\}. \tag{2.6}$$

The $1/e^2$ radius w_0 and the wavelength λ are the only independent parameters. All other quantities are defined as

$$k = \frac{2\pi}{\lambda} \qquad \text{(Wave vector)}$$

$$z_\text{R} = \frac{\pi w_0^2}{\lambda} \qquad \text{(Rayleigh length)}$$

$$w(z) = w_0 \sqrt{1 + \left(\frac{z}{z_\text{R}}\right)^2} \qquad (1/e^2 \text{ radius})$$

$$R(z) = z\left\{1 + \left(\frac{z_\text{R}}{z}\right)^2\right\} \qquad \text{(Radius of curvature)}$$

$$\zeta(z) = \arctan\left(\frac{z}{z_\text{R}}\right). \qquad \text{(Gouy phase shift)}$$

Thus, the intensity distribution for the running wave configuration is given by

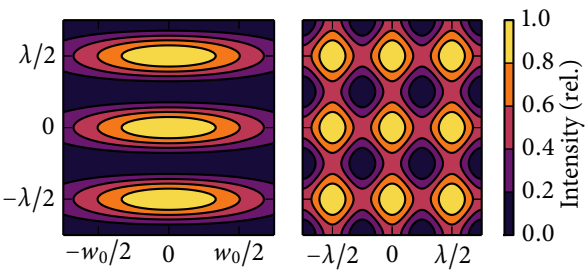

FIGURE 2.4: Optical lattice geometries for a single (left) and two standing waves where the k-vectors enclose an angle of $\pi/2$ (right). The resulting potential is plotted in the plane defined by the two k-vectors. We assume the two laser beams are detuned.

$I(r,z) \equiv |E(r,z)|^2$ with

$$I(r,z) = I_0\left(\frac{w_0}{w(z)}\right)^2 \exp\left(-\frac{2r^2}{w^2(z)}\right). \tag{2.7}$$

For small r and z we can expand $I(r,z)$ around $r = 0, z = 0$

$$I(r,z) = I_0\left\{1 - 2\left(\frac{r}{w_0}\right)^2 - \left(\frac{z}{z_R}\right)^2\right\} + \mathcal{O}(r^2z^2) + \mathcal{O}(r^2) + \mathcal{O}(z^2). \tag{2.8}$$

Thus, we can approximate the intensity distribution and the resulting potential as a harmonic potential around $r = 0, z = 0$. For atoms that are close to the trap bottom the trapping potential looks nearly harmonic. This is the case for sufficiently cold atoms in the lower states of the quantum harmonic oscillator. Figure 2.3 shows a plot of the exact potential and the harmonic approximation for the running wave configuration.

The standing wave configuration is given by two overlapping Gaussian beams with $\vec{k}$ vectors, which point in opposite directions. The two beams are otherwise identical and we can simply generate this configuration by retro-reflecting a focused laser beam. The resulting intensity distribution I_{sw} defined by the interference pattern between the two electric fields E_- and E_+ is given as

$$\begin{aligned} I_{\mathrm{sw}} &= |E_-(r,z) + E_+(r,z)|^2 \\ &= E_-(r,z)E_+^*(r,z) + E_-^*(r,z)E_+(r,z) + \left|E_-(r,z)\right|^2 + \left|E_+(r,z)\right|^2 \\ &= 4\,\underbrace{I_0\left(\frac{w_0}{w(z)}\right)^2 \exp\left(-\frac{2r^2}{w^2(z)}\right)}_{(*)} \cdot \underbrace{\cos^2\left(kz - k\frac{r^2}{2R(z)} - 2\zeta(z)\right)}_{(**)}. \end{aligned} \tag{2.9}$$

We can neglect the Gouy phase shift for $z \ll z_{\mathrm{R}}$. Close to $r = 0$ the term (**) is given as $\cos^2(kz) \approx 1 - k^2z^2$ around every $z = \pi(2n-1)/2k$ with $n \in \mathbb{Z}$. The overall intensity distribution is then given by the fast modulation described by the term (**) and the envelope given in the term (*). We find a result similar to the harmonic approximation in the transverse direction of the running wave configura-

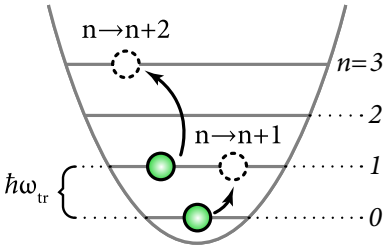

FIGURE 2.5: Illustration of heating processes in a harmonic potential. Atoms that make $n \rightarrow n + j$ with $j > 0$ transition contribute to an increase of the total energy. We call this parametric heating for $j = 2$ and dipole heating for $j = 1$.

tion. However, in the longitudinal direction there is separate harmonic potential at every half-wavelength. This is an one-dimensional optical lattice, which is plotted in Figure 2.3. When multiple one-dimensional lattices are overlapped, two- and three-dimensional lattices are generated. A two-dimensional plot of the resulting potential is shown in Figure 2.4.

2.3 LASER NOISE AND HEATING

In general, potentials for optical traps are generated by laser beams. Thus, we are interested in what influence laser noise has on the atoms in the quasi-harmonic trap. We are specifically interested in atom heating due to presence of noise in the light field. Heating puts limits on the minimum achievable temperatures as well as the lifetime in the trap and thereby on the physics we can observe in our experiment. We derive the heating rate for intensity and pointing noise in detail and discuss the special case of optical dipole potentials against gravity. Results from our actual laser setup are discussed at the end of this section.

We have established a basic understanding of the potentials in running and standing wave optical dipole traps in the last section. This allows us to estimate how noise from the laser contributes to heating of the trapped atoms. As long as the atoms are sufficiently cold to occupy mainly the low motional states, the physics should be well described by the quantum harmonic oscillator Hamiltonian [5],

$$H = \frac{p^2}{2M} + \frac{1}{2}M\omega_{\mathrm{tr}}^2 x^2. \tag{2.10}$$

Here, M is the mass of a single atom and

$$\omega_{\mathrm{tr}}^2 = \begin{cases} 2\mathrm{Re}(\alpha)I_0/(Mz_{\mathrm{R}}^2) & \text{(longitudinal)} \\ 4\mathrm{Re}(\alpha)I_0/(Mw_0^2) & \text{(transverse)} \end{cases} \tag{2.11}$$

is the trapping frequency defined in terms of the maximum intensity I_0, the atomic polarizability α, and the Rayleigh length z_{R} respectively the $1/e^2$ beam radius w_0. The eigenstates of H are denoted by $|n\rangle$ and their energy by E_n.

Heating describes an increase in the total energy stored in the motional degree of freedom, i.e. atoms move to higher harmonics oscillator levels over time. The two types of laser noise we consider here are intensity noise and pointing noise. Intensity noise modulates the effective intensity at time t whereas pointing noise modulates the effective trap center defined by $x = 0$ at time t. Pointing noise is passively minimized by using mechanically stable optics or transformed into intensity noise by using optical fibers. Intensity noise is mostly determined by the type of laser and must be actively minimized if too high. A theoretical description of laser noise induced heating was first given in Ref. [7]. We follow the same approach to derive the heating rates of intensity and pointing noise but provide a comprehensive derivation.

A. HEATING DUE TO INTENSITY NOISE

First, we consider heating due to intensity noise. Let I_0 be the average intensity, $I(t)$ the time-dependent intensity, and let $\epsilon(t)$ describe the relative intensity fluctuations,

$$\epsilon(t) \equiv \frac{I(t) - I_0}{I_0}. \tag{2.12}$$

The time dependent Hamiltonian is then given as

$$H(t) = \underbrace{\frac{p^2}{2M} + \frac{1}{2}M\omega_{\mathrm{tr}}^2 x^2}_{H_0} + \underbrace{\frac{1}{2}M\omega_{\mathrm{tr}}^2 \epsilon^2(t) x^2}_{H'(t)}. \tag{2.13}$$

Assume the atom is initially in the state $|n\rangle$. Then we are interested in the average transition rate $W_{m\leftarrow n}$ from state $|n\rangle$ to state $|m \neq n\rangle$. We assume that the population of different harmonic oscillator states is constant within time T, which is much larger than the correlation time of the fluctuations $\epsilon(t)$. First-order time-dependent perturbation theory yields then

$$\begin{aligned} W_{m\leftarrow n} &= \frac{1}{T}\frac{1}{\hbar^2}\left|\int_0^T dt\, \langle m|\, H'(t)\, |n\rangle \exp\left\{\frac{i}{\hbar}\left(E_m - E_n\right)t\right\}\right|^2 \\ &= \frac{M^2\omega_{\mathrm{tr}}^4}{4\hbar^2}\frac{1}{T}\int_0^T dt \int_0^T dt' \left\{\epsilon(t)^* \epsilon(t')\right\} \left|\langle m|\, x^2\, |n\rangle\right|^2 \exp\left\{i\omega_{m\leftarrow n}\left(t - t'\right)\right\}. \end{aligned} \tag{2.14}$$

The term $\epsilon(t)^*\epsilon(t')$ and the power spectral density (PSD) $\tilde{S}_\epsilon(\omega)$ are related by the Fourier transform[1]

$$\tilde{S}_\epsilon(\omega) = \lim_{T\to\infty} \frac{1}{2\pi T}\int_0^T dt \int_0^T dt' \left\{\epsilon(t)^* \epsilon(t')\right\} \exp\left\{i\omega(t - t')\right\}. \tag{2.15}$$

[1] This is a special case of the *Wiener-Khinchin Theorem*, see Ref. [8, p. 371] for a proof.

We can use this relation to rewrite the transition probability in terms of the PSD of the noise. Note that $\epsilon(t)^* \epsilon(t')$ has only real values and the Fourier transform is symmetric to its conjugate. Thus it is practical to introduce the one-sided power spectral density $S_\epsilon = 2\tilde{S}_\epsilon$. If the noise is uncorrelated, i.e. $\epsilon(t)^* \epsilon(t+\tau) = 0$ for $\tau \ll T$, then T can be extended to ∞ and

$$W_{m \leftarrow n} = \frac{M^2 \omega_{\mathrm{tr}}^4 \pi}{4\hbar^2} \left| \langle m | \, x^2 \, | n \rangle \right|^2 S_\epsilon \left(\omega_{m \leftarrow n} \right). \tag{2.16}$$

This result is especially useful since we can easily measure the PSD of the intensity noise on the laser using a photodetector. Using the identity $x = \sqrt{\hbar / 2M\omega_{\mathrm{tr}}} \left(a + a^\dagger \right)$ for the x operator, the term $\left| \langle m | \, x^2 \, | n \rangle \right|^2$ evaluates to:

$$\left| \langle m | \, x^2 \, | n \rangle \right|^2 = \frac{\hbar^2}{4M^2 \omega_{\mathrm{tr}}^2} \left\{ \delta_{m,n-2} n(n-1) + \delta_{m,n+2} (n+1)(n+2) \right\} \tag{2.17}$$

with $\delta_{i,j} = 1$ if $i = j$ and 0 otherwise. The term $\left| \langle m | \, x^2 \, | n \rangle \right|^2$ vanishes unless $m = n \pm 2$. Thus, we observe transitions for $\Delta n = 2$, which corresponds to intensity fluctuations at $2\omega_{\mathrm{tr}}$. This is a *parametric* process, which is fundamentally different from the resonance at ω_{tr} when driving the harmonic oscillator directly. This is similar to squatting and standing up on a swing at twice the resonant frequency[2].
We now find the corresponding transition rates

$$\begin{aligned} W_{n \pm 2 \leftarrow n} &= \frac{\pi}{16} \omega_{\mathrm{tr}}^2 S_\epsilon \left(\omega_{n \pm 2 \leftarrow n} \right) (n + 1 \pm 1)(n \pm 1) \\ &= \frac{\pi}{16} \omega_{\mathrm{tr}}^2 S_\epsilon \left(2\omega_{\mathrm{tr}} \right) (n + 1 \pm 1)(n \pm 1). \end{aligned} \tag{2.18}$$

The heating rate is now given by the average change in energy $\langle \dot{E} \rangle$ due to transitions $n \rightarrow n \pm 2$. Let $p(n)$ be the occupation probability for state $|n\rangle$ at time t and we find,

$$\begin{aligned} \langle \dot{E} \rangle &= \sum_n p(n) \underbrace{2\hbar\omega_{\mathrm{tr}} \left(W_{n+2 \leftarrow n} - W_{n-2 \leftarrow n} \right)}_{\text{Rate of energy change per state } |n\rangle} \\ &= \sum_n p(n) \, 2\hbar\omega_{\mathrm{tr}} \frac{\pi}{16} \omega_{\mathrm{tr}}^2 S_\epsilon \left(2\omega_{\mathrm{tr}} \right) (4n + 2) \\ &= \underbrace{\left\{ \sum_n p(n) \, \hbar\omega_{\mathrm{tr}} \left(n + \frac{1}{2} \right) \right\}}_{\langle E \rangle} \frac{\pi}{2} \omega_{\mathrm{tr}}^2 S_\epsilon \left(2\omega_{\mathrm{tr}} \right) \\ &= \langle E \rangle \, \frac{\pi}{2} \omega_{\mathrm{tr}}^2 S_\epsilon \left(2\omega_{\mathrm{tr}} \right) = \langle E \rangle \, \pi^2 \nu_{\mathrm{tr}}^2 S_\epsilon \left(2\nu_{\mathrm{tr}} \right). \end{aligned} \tag{2.19}$$

Thus, the energy changes exponentially with rate $\Gamma \equiv \pi^2 \nu_{\mathrm{tr}}^2 S_\epsilon \left(2\nu_{\mathrm{tr}} \right)$. It depends quadratically on the trapping frequency ν_{tr} and intensity fluctuations at $2\nu_{\mathrm{tr}}$.

[2] People do this on a *Russian swing*, see http://en.wikipedia.org/wiki/Russian_swing.

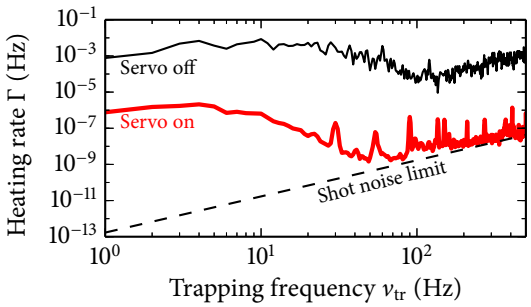

FIGURE 2.6: Heating rate of atoms in light from the 1064 nm laser setup as a function of trapping frequency. The two traces show the heating rate with intensity servo turned on (thick, red) and off (thin, black). The shot noise limit indicates the heating rate for an intensity servo with infinite gain.

B. HEATING DUE TO POINTING NOISE

We can find an expression for pointing noise analogous to the derivation of Eqn. 2.19 in the previous section. Let $\chi(t)$ be the parameter that characterizes the fluctuations of the trap center around $x = 0$. Then the resulting time-dependent Hamiltonian is given as

$$H(t) = \underbrace{\frac{p^2}{2M} + \frac{1}{2}M\omega_{\mathrm{tr}}^2 x^2}_{H_0} - \underbrace{M\omega_{\mathrm{tr}}^2 x\chi(t)}_{H'(t)} + \mathcal{O}\left\{\chi^2(t)\right\}. \tag{2.20}$$

Analogous to the previous derivation we use first order perturbation theory to derive an expression for the average transition rate $W_{m\leftarrow n}$

$$W_{m\leftarrow n} = \frac{M^2\omega_{\mathrm{tr}}^4}{2\hbar^2}\frac{1}{T}\int_0^T dt \int_0^T dt' \left\{\chi(t)^* \chi(t')\right\} |\langle m| x |n\rangle|^2 \exp\left\{i\omega_{m\leftarrow n}\left(t - t'\right)\right\}. \tag{2.21}$$

Again, letting $T \to \infty$ and introducing the one-sided PSD $S_\chi(\omega)$ of the pointing noise yields

$$W_{m\leftarrow n} = \frac{M^2\omega_{\mathrm{tr}}^4\pi}{\hbar}|\langle m| x |n\rangle|^2 S_\chi\left(\omega_{m\leftarrow n}\right). \tag{2.22}$$

The term $|\langle m| x |n\rangle|^2$ evaluates to

$$|\langle m| x |n\rangle|^2 = \frac{\hbar}{2M\omega_{\mathrm{tr}}}\left\{n\delta_{m,n-1}, +(n+1)\delta_{m,n+1}\right\}. \tag{2.23}$$

Thus, the term $|\langle m| x |n\rangle|^2$ vanishes unless $m = n \pm 1$. Thus, we observe transition for $\Delta n = 1$. This corresponds to directly driving the harmonic oscillator at the resonant frequency ω_{tr}, which is different from parametric heating due to intensity noise.

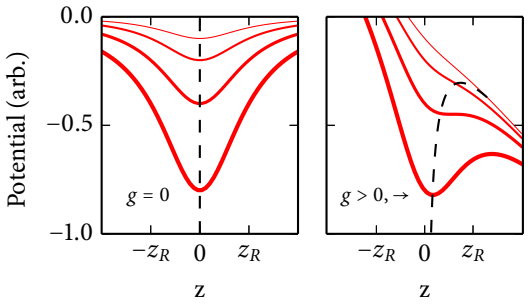

FIGURE 2.7: Optical dipole trap center without (left) and with (right) gravity for different potential depths as a function of the Rayleigh length z_R. The dashed black lines indicate the local minimums of the potentials.

Analogous to Eqn. 2.19 we find the resulting heating rate as

$$\begin{aligned}\langle \dot{E} \rangle &= \sum_n p(n)\, \hbar\omega_{\mathrm{tr}} \left(W_{n+1\leftarrow n} - W_{n-1\leftarrow n} \right) \\ &= \underbrace{\left\{ \sum_n p(n) \right\}}_{=1} \frac{\pi}{2} M \omega_{\mathrm{tr}}^4 S_\chi \left(\omega_{\mathrm{tr}} \right) \\ &= \frac{\pi}{2} M \omega_{\mathrm{tr}}^4 S_\chi \left(\omega_{\mathrm{tr}} \right) = 4\pi^4 M \nu_{\mathrm{tr}}^4 S_\chi \left(\nu_{\mathrm{tr}} \right).\end{aligned} \tag{2.24}$$

Thus, the energy changes linearly with the rate $\xi = 4\pi^4 M \nu_{\mathrm{tr}}^4 S_\chi \left(\nu_{\mathrm{tr}} \right)$ and depends on the fourth power of the trapping frequency ν_{tr}, the pointing noise at ν_{tr}, and the atomic mass M.

Last, we consider a harmonic optical dipole potential under gravity, which yields the following Hamiltonian:

$$H(t) = \frac{p^2}{2M} + \frac{1}{2} M \omega_{\mathrm{tr}}^2 x^2 - gMx \tag{2.25}$$

Here $g > 0$ is a constant. This potential has not a global but a local minimum at $x = g/\omega_{\mathrm{tr}}^2$. This minimum is a function of the trapping frequency, which depends on the intensity (see Eqn. 2.11). Thus, intensity fluctuations can introduce trap center fluctuations, which in turn introduce heating as described in the previous section. The shift of the trap minimum as a function of intensity is shown in Figure 2.7.

In this section we have derived the heating rates for intensity and pointing noise in harmonic optical dipole traps. Intensity noise causes exponential growth, whereas pointing noise causes linear growth of the motional energy. Further we have shown how intensity noise on a combination of a harmonic and linear potential leads to trap center fluctuations similar to those caused by pointing noise. These results motivate the intensity servo described in Section 4.1.

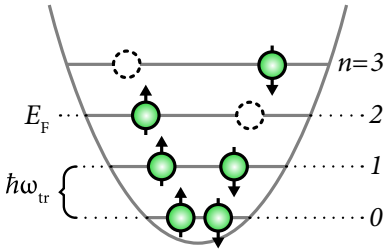

FIGURE 2.8: Illustration of the Fermi energy E_F in an one dimensional harmonic potential with spin-1/2 fermions. The lower three states are filled up except for one fermion, which is excited in the $n = 3$ level.

2.4 FERMIONS IN HARMONIC POTENTIALS

We trap strontium-87 atoms in optical dipole traps, which essentially are three-dimensional harmonic potentials. Therefore it is important how quantities like phase-space density scale for fermions in those potentials. This section mainly summarizes results from Ref. [9]. The interested reader can consult the reference for detailed explanations.

First, we define a generalized three-dimensional harmonic potential, which could be realized by one or multiple optical dipole trap potentials. Let $\vec{r} = (x_1, x_2, x_3)$ where x_i are three orthogonal directions in Cartesian space.

$$V(\vec{r}) = \frac{1}{2} M \sum_i \omega_i^2 x_i^2 \tag{2.26}$$

Here M is the mass of the atoms and ω_i is the trapping frequency along the direction $\hat{x}_i$. We define the (geometric) mean trap frequency $\overline{\omega}$ as

$$\overline{\omega} = \left(\prod_i \omega_i \right)^{1/3} . \tag{2.27}$$

Fermions obey the Pauli exclusion principle, i.e. two fermions can not occupy the same quantum state in a closed system. This is described with the Fermi-Dirac distribution, which gives the average number of fermions in the energy eigenstate E_i as

$$\langle n_i \rangle = g_i \, / \{ \exp(\beta [E_i - \mu]) + 1 \} . \tag{2.28}$$

Here $g_i \in \mathbb{N}$ is the degeneracy of the state, $\beta^{-1} \equiv k_B T$, and μ is the chemical potential. The chemical potential can be calculated from $\mu = \frac{\partial G}{\partial N}\big|_{T,P}$ where G is the Gibbs free energy. The resulting phase space density distribution for an atom in the potential described above is then given as,

$$f(\vec{r}, \vec{p}) = g \Big/ \left\{ \exp\left(\beta \left[\frac{p^2}{2M} + V(\vec{r}) - \mu \right] \right) + 1 \right\} . \tag{2.29}$$

Here g is the degeneracy of a single state in the three dimensional harmonic potential given by $V(\vec{r})$. This is usually given in terms of the available spin states, e.g. $g = 10$ for the ground state of strontium-87. Let

$$N = \int \frac{d^3\vec{r}\, d^3\vec{p}}{2\pi\hbar^2}\, f(\vec{r},\vec{p}) \tag{2.30}$$

be the total number of atoms in the harmonic potential. At $T = 0$, the atoms are in the lowest possible energy configuration where all N/g lowest states of the potential $V(\vec{r})$ are filled up to the energy E_F. We call this energy the *Fermi energy*, which is given as [9],

$$E_\mathrm{F} = \hbar\overline{\omega}(6N/g)^{1/3}. \tag{2.31}$$

For the approximations in this section we assume that the Fermi energy E_F is much larger than the energy splittings $h\omega_i$ of the three-dimensional harmonic potential. The *Fermi temperature* is defined as $T_\mathrm{F} = E_\mathrm{F}/k_\mathrm{B}$. From Eqn. 2.28 we directly find that μ must be equal to E_F at $T = 0$ to reproduce the distribution expected from the Pauli exclusion principle. The atom number density n as a function of $\vec{r}$ is given as [9]

$$\begin{aligned} n(\vec{r}) &= \int \frac{d^3\vec{p}}{2\pi\hbar^2}\, f(\vec{r},\vec{p}) \\ &= \frac{g}{\lambda_\mathrm{dB}^3}\mathrm{Li}_{3/2}\left(\exp\left\{\beta\left[\frac{p^2}{2M} + V(\vec{r}) - \mu\right]\right\}\right). \end{aligned} \tag{2.32}$$

Here, $\mathrm{Li}_{3/2}$ is a polylogarithm with $\mathrm{Li}_{3/2}(x) = 1/\Gamma(3/2)\int_0^\infty dq\, q^{1/2}/(e^q/x - 1)$, and

$$\lambda_\mathrm{dB} = \sqrt{2\pi\beta\hbar^2/M} \tag{2.33}$$

is the de Broglie wavelength. The high temperature limit of $n(\vec{r})$ is the Maxwell-Boltzmann distribution.

In this section, we have discussed the density for fermions in a harmonic trap. Furthermore, important quantities like the Fermi energy have been defined. This helps to evaluate the experimental data in Chapter 5.

3

EXPERIMENTAL APPARATUS

This chapter explains the experimental apparatus, including the UHV chamber and laser systems used to trap, cool, and manipulate strontium-87 atoms. We give a short overview of the new UHV chamber, magnetic coils, strontium oven, and the blue and red laser systems. The author was mainly involved in the 1064 nm and 813 nm laser systems, which are discussed separately in Section 3.2 and Section 3.3.

3.1 OVERVIEW

The experiment uses a UHV chamber, which is shown in Figure 3.1. The chamber has good optical access with two large viewports in the vertical and 13 viewports in the horizontal plane. The chamber is connected to several pumps: Two ion pumps, a non-evaporative getter pump, a titanium sublimation pump, and a getter coating on the inside of the chamber (titanium-zirconium-vanadium). The pressure is 1×10^{-11} Torr with the atomic beam oven turned on.

Two water-cooled magnetic coils in an anti-Helmholtz configuration generate the quadrupole field required for the MOT. The main chamber has recessed windows on the top and bottom, which allow the magnetic coils to be placed relatively close to the atoms. The maximum field gradient at the atoms is ≈ 550 G/cm. Three Helmholtz pairs of bias field coils are used to cancel the background magnetic field and define the point of zero field inside the chamber. This allows us to move the MOT and align it to the laser beams.

We use an integrated atomic beam oven and Zeeman slower from AOSense, which features a very compact design (see Figure 3.1) and does not need any water cooling due to the use of permanent magnets in the Zeeman slower. The integrated oven and Zeeman slower features in-vacuum optics, which allow us to get a 2D MOT by coupling light into just one window. The atomic beam is steered towards the main

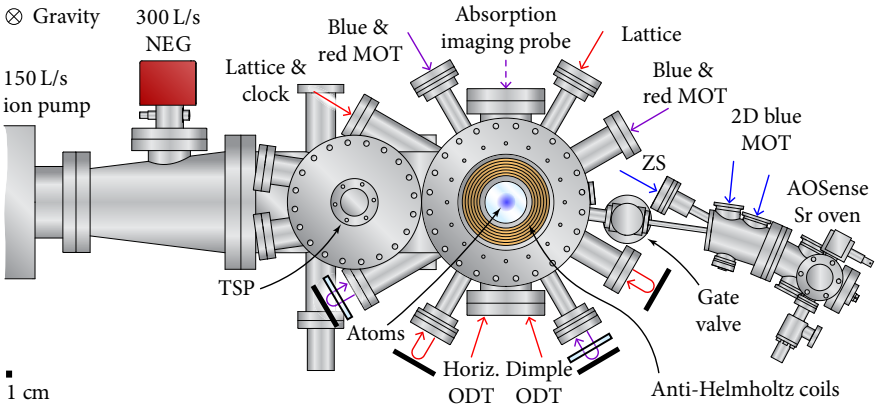

FIGURE 3.1: UHV chamber with main beam paths (arrows) and vacuum pumps. Combined blue and red laser light is shown in purple. The vertical MOT, vertical lattice, vertical optical dipole trap, and vertical imaging beam are not shown in this drawing. Those beams are launched through the bottom and top viewport at nearly normal angle of incidence.

chamber at an angle using a second 2D MOT. Thus, the atomic beam can be "shut off" by blocking the light for the 2D MOT. We operate the oven at 460 °C, which gives an atom flux of $\approx 2 \times 10^{13}$ atoms/s.

Most of the optics are on separate breadboards and laser light is delivered to the atoms by optical fibers. This maps pointing noise on the side of the laser setup to intensity fluctuations on the side of the atoms. We can then simply stabilize the intensity and reduce the overall noise. See Section 4.1 for a detailed description of the intensity servo scheme used. An additional advantage of the separate breadboards is that in the event of laser failure only the optics on the side of the laser setup need to be realigned. The beam splitting, shaping, and polarizing optics are mounted on a mezzanine, which is a ≈ 6 cm thick steel breadboard that is mounted on 25.4 cm high aluminum posts that are filled with lead shot. This allows all the optics to be on the same height as the atoms in the chamber. Most optics are mounted on short fixed-height steel posts to minimize drift.

The laser systems for the red and blue MOT have already been used for the old experiment. The red laser system uses a master ECDL locked to an ultra-stable cavity and two slaves, which are phase locked to the master. The blue laser system uses a master ECDL locked to a hollow cathode lamp and slave free running diode lasers, which are injection locked to the master.

3.2 THE 1064 NM LASER SETUP

The 1064 nm laser setup delivers high power light for the optical dipole trap. Figure 3.11 shows the main setup and Figure 3.13 shows the optics on the mezzanine. The first two sections discuss the seed laser/fiber amplifier and the photonic crystal fibers used to deliver high power from the main setup to the atoms.

A. SEED LASER AND FIBER AMPLIFIER

We use a seed and amplifier configuration to generate high optical power at 1064 nm as shown in Figure 3.11. The seed laser is a 500 mW diode-pumped Nd:YAG laser with a monolithic design, which allows narrow linewidth and relatively high power. Light from the seed laser is amplified using a 50 W fiber amplifier from Nufern. The Nufern amplifies 1 – 15 mW of seed light to a maximum output of 50 W[1]. This section explains the basic operating principle of the seed laser and the amplifier, which helps to understand shortcomings and specific features of the laser setup.

The Nd:YAG laser is based on the MISER (Monolithic isolated single-mode end-pumped ring) design. This design uses a non-planar ring cavity, which is formed by the Nd:YAG crystal itself. Figure 3.2 shows the beam path inside the crystal. This design was first realized in Ref. [10] and has several advantages:

- High mechanical/thermal stability because the monolithic design prevents any differential drift of other optics with respect to the crystal.
- The beam inside the MISER cavity is a running wave. This prevents spatial hole burning, which is the effect where spatially modulated gain in a planar cavity leads to oscillations of higher order modes.

There are some technical caveats to make the laser truly unidirectional and the output polarization linear. When a magnetic field is applied to the Nd:YAG, the Faraday effect leads to a k-vector dependent rotation of the polarization. This allows the laser

[1]The specifications from the manufacturer quote a maximum power of 50 W output power. However, it was only operated/tested up to ≈ 40 W in our setup.

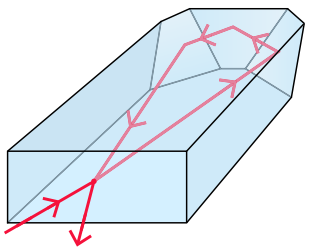

FIGURE 3.2: Monolithic isolated single-mode end-pumped ring (MISER) crystal design. The pump beam enters the crystal on the front surface, is reflected on the angled back surface on the right, the top surface, and finally on the left angled back surface before exiting the cavity again through the front surface. Note that the non-planar beam path introduces a slight rotation of the polarization. *Drawing adapted from Ref. [10, Fig. 1]*

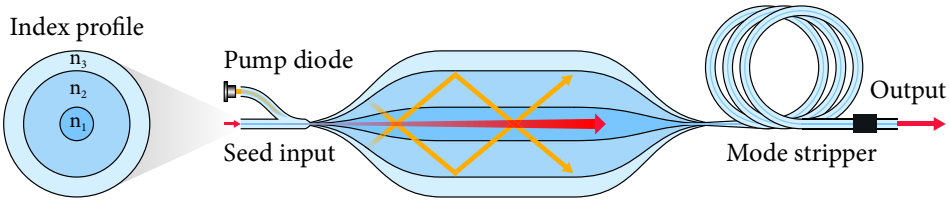

FIGURE 3.3: Basic operating principle of a fiber amplifier following the description in [6]. The index profile is shown on the left. The inner core has refractive index n_1, the outer core n_2, and the outer cladding n_3. Light from the pump diode (orange) is coupled into the outer cladding whereas light from the seed (red) is coupled into the quasi-single-mode core. The expanded cross-section of the fiber is shown in the middle. Light from pump passes through the inner core and pumps rare-earth ions leading to amplification of the light as it travels from left to right. The coil on the right is used to strip any higher modes from the quasi single-mode core. The mode stripper at the output removes any remaining power in the outer core.

to operate unidirectionally. A dielectric coating on the out-coupling surface is made less transmissive for one polarization, which introduces polarization selectivity. The interested reader might consult Ref. [10] for an excellent and detailed explanation.

However, the maximum power (up to 2 W lasers are commercially available) for this design is limited by thermal lensing. As the pump power is increased, the Nd:YAG crystal heats non uniformly along the transverse direction of the beam path. This leads to a non-uniform modulation in the optical path length and to a mode mismatch, i.e. the output is not single-mode anymore [11]. Thus, we use a fiber laser amplifier to amplify the signal from the 500 mW Nd:YAG laser.

The fiber amplifier (Nufern NuAmp 50 W) uses a double cladded active fiber to amplify light from input powers on the order of a few milliwatts to output powers of $\approx$ 50 W. The fiber has an inner core and an outer core with diameter on the order of 10 µm and 100 µm, respectively. Additionally, a second cladding - the outer cladding - surround the inner cladding. This forms two fiber interfaces:

1. The inner core together with the inner cladding forms a single-mode fiber[2] with a low NA. The seed laser is coupled into this single-mode fiber.

2. The outer core together with the outer cladding forms a multi-mode fiber with a large NA. This allows the coupling of light from multiple pump diodes into the fiber and reaching high optical powers.

The inner core of the fiber is doped with Ytterbium 3+ ions that can be pumped

[2] Actually, the inner core can also be multi-mode, but the NA has to be small enough to allow significant bend-loss for higher order transverse modes [12, p. 371]. The fiber can then be coiled and still operate single mode while allowing for a larger mode area and therefore lower peak intensity, which limits the overall maximum output power.

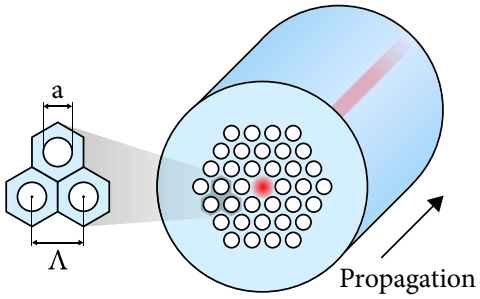

FIGURE 3.4: Structure of a photonic crystal fiber fiber with the hole diameter a and hole spacing Λ. The unit cells are hexagons of which three are shown on the left. Light propagates in the defect at the center of the fiber along the longitudinal direction (red beam at the center).

between 800 nm and 1064 nm and can emit at 1064 nm (in silica) [13]. This allows the inner core to act as the gain medium. While the light from the seed laser determines the phase and wavelength of the output light, the high intensity light from the pump laser diodes allows a large gain (up to 46 dB for our amplifier). A mode stripper at the output end of the fiber strips the higher-order modes in the outer core and turns the excess optical power into heat. Figure 3.3 shows the basic operating principle of the fiber laser. The single mode with high intensity at the output can then be collimated using a lens. The mode quality of the out-coupled beam is very good compared to the mode of a laser diode. The fiber amplifier is thermally stabilized using a chiller (setpoint at 23 °C) to prevent excess heat induced damages.

B. PHOTONIC CRYSTAL FIBERS

We use photonic crystal fibers to deliver power from the 1064 nm laser system to the atoms. This section describes limitations of standard step-index fibers for high laser power and explains how photonic crystal fibers can overcome these limitations.

For high optical powers, dielectric materials show electrostriction – an effect that causes the local density to be modulated[3] by the electric field strength [14]. This is the origin of stimulated Brillouin scattering (SBS) in optical fibers. Acoustic noise - present in all fibers - can make forward-traveling photons scatter into a phonon and a backwards-traveling photon (of slightly different frequency)[4]. This forms an interference pattern in the fiber that modulates the density and this acoustic wave further enhances back-scattering, so this is a stimulated process. SBS is a non-linear process and there exists a threshold where the back-scattered power becomes comparable to the input power. This threshold depends on the fiber length, dielectric material, core diameter, and the wavelength of the incident light [14]. For a 5 m step-index, single-mode (fused silica) fiber with a 5 µm core, and 1064 nm light the threshold is given by ≈ 2.75 W using the approximation given in Ref. [15]. These parameters are typical of those for other fibers in the experiment.

When using step-index fibers for high power delivery, it is necessary to increase

[3] The modulation strength is proportional to the intensity of the electric field.
[4] Forward scatter is of course also possible but less likely.

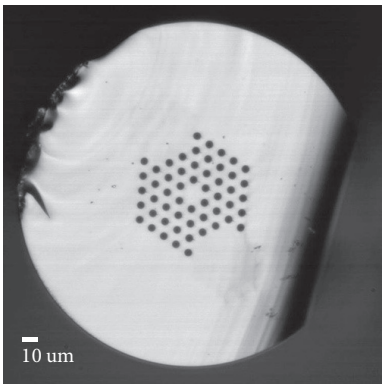

FIGURE 3.5: Microscopic image of the Holey fiber (NKT Photonics LMA-PM-15) used in the experiment. The scale is based on the measurements given in the datasheet (OD of cladding given as 230 µm ± 5 µm [16]). Stress rods are vaguely visible on the top left and bottom right. This allows this fiber to be polarization maintaining. The contrast of the image is slightly increased to provide better visibility of the different features.
Image kindly provided by NKT Photonics/USA.

the SBS threshold value. The straight-forward approach would be to to increase the core diameter, i.e. reduce the peak power density inside the fiber. But, we want to maintain single-mode operation. The constraint for single-mode operation of a step-index fiber is given as [6, p. 337],

$$V = \frac{\pi a}{\lambda_0} \underbrace{\left(n_{\text{core}}^2 - n_{\text{cladding}}^2\right)^{1/2}}_{\text{NA}} \leq 2.405. \tag{3.1}$$

Here, a is the fiber core diameter and λ_0 the wavelength of interest. The V-parameter is defined in terms of the number of modes N_{m} [6, p. 338]

$$N_{\text{m}} \approx \frac{4}{\pi^2} V^2. \tag{3.2}$$

Thus, for larger a, the NA has to be reduced to maintain single-mode operation. However, decreasing the NA far below 0.07 leads to significant bend loss rendering the fiber useless. Therefore standard step-index fiber cannot be used to deliver high power single-mode laser light.

Photonic crystal fibers consist of a solid single-material (usually fused silica) fiber that has a two-dimensional periodic structure of air gaps on the plane transverse to light propagation. The fiber we use has a triangular pattern of circular hole with a defect at the center. This particular type of fiber is called the *Holey fiber*. The structure is shown in Figure 3.4 and a microscopic image of the cross-section is shown in Figure 3.5. The Holey fiber has an effective V-parameter V_{eff} (for which Eqn. 3.1 applies) given as [17]

$$V_{\text{eff}} = \frac{2\pi}{\lambda_0} \Lambda F^{1/2} \left(n_0^2 - n_{\text{air}}^2\right)^{1/2}. \tag{3.3}$$

Here, n_0 is the refractive index of the fiber material, Λ is the spacing between neighboring holes (see Figure 3.4), and F is the air filling fraction of a (hexagonal) unit

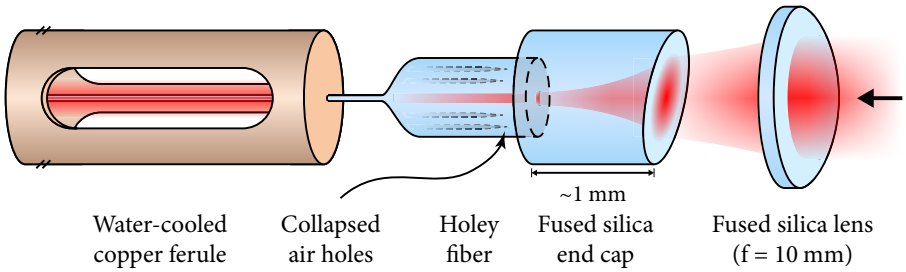

FIGURE 3.6: High-power fiber connector with different features and a focused laser beam entering the fiber from the right. The glowing fiber in the copper ferrule shows the escape of miscoupled light from the fiber. Note that none of this schematic is to scale and part of the Holey fiber as well as the end cap are magnified to make the details visible. An additional glass ferrule for protection of the delicate fiber is not shown in the drawing. Compare with the photo of the connector in Figure 3.7 for the relative sizes of the all features.

cell, given as

$$F = \pi \left(\frac{a}{2}\right)^2 \Big/ \left(\frac{\sqrt{3}}{2}\Lambda^2\right) = \frac{\pi}{\sqrt{32}}\left(\frac{a}{\Lambda}\right). \tag{3.4}$$

Here a is the diameter of a circular hole in the unit cell (see Figure 3.4). The light travels in the defect at the center of the fiber and the mode area is approximately proportional to Λ/a [17]. This allows us to increase the mode area by choosing large spacing Λ and a relatively small hole diameter a while maintaining single-mode operation in terms of Eqn. 3.1 [18]. Thus, the SBS threshold is higher and the Holey fiber can deliver high-power single-mode laser light. This solves the problem described in the previous paragraph. The periodic holes in the fiber "cladding" of the Holey fiber present a band gap for the fundamental mode so it cannot exist outside the center defect region. However, higher order modes can exit the core. They can simply escape the defect at the center of the fiber and propagate to the outside of the fiber [17]. Thus, only the fundamental mode is guided, whereas significant loss for higher order modes is introduced. The fundamental mode of the Holey fiber has a similar intensity profile as a Gaussian. Figure 3.8 shows the far field intensity distribution of the Holey fiber used in the experiment. Holey fibers are made from pure fused silica compared to doped fused silica in standard step-index fibers. This is another advantage as defects and undesired scattering are reduced.

We use the Holey fiber LMA-PM-15 from NKT Photonics. It has a $1/e^2$ mode diameter of 12.6 µm ± 1.5 µm at 1064 nm and is made from pure fused silica [16]. We use a special high power connector (HP2.5 from Tratech Fiberoptics) to prevent damage of the fiber surface and the fiber in general. The connector design, shown in Figure 3.6, has several features to prevent damage of the fiber and allow transmission of high optical powers:

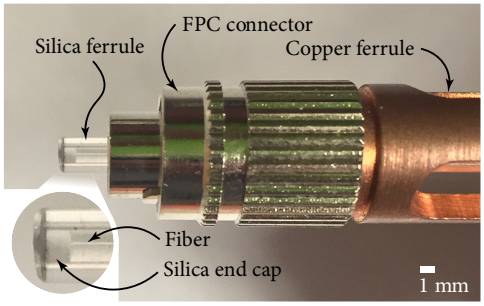

FIGURE 3.7: Photo of the high-power fiber connector. The inset on the bottom left shows a magnification of the fiber tip and silica end cap. The copper ferrule as well as the cut-outs are visible on the right.

- The Holey fiber is fused to a solid silica end cap of 1 mm ± 100 µm length. The laser beam continues to focus down onto the fiber tip inside the end cap (see Figure 3.6). This allows a larger mode diameter and correspondingly a lower power density on the air to end cap interface than it would be possible on an air to fiber tip interface. This makes the fiber connector less likely to be damaged due to surface defects or trapped dust particles.
- The fiber end cap and Holey fiber are in good thermal contact with a copper ferrule. This allows us to cool heat from miscoupled light.
- Cutouts in the copper ferrule allow miscoupled light to exit the ferrule without causing more heating. This is actually visible on an IR viewer (we are using the fibers with 1064 nm light).

We use a custom-made copper block that holds the copper ferrule of the fiber connector for water-cooling. Thermocouples connected to the copper ferrule close to the fiber tip allow continuous monitoring of the fiber temperature and will be connected to the interlock, which can redirect the high-power laser beam to a beam dump using an AOM. With no light the fibers are at a temperature of ≈ 17.5 °C, which is relatively close to the mean water temperature of ≈ 16 °C. When operating the fiber at high power (i.e. ≥ 12 W) the temperature can rise to up to 22 °C depending on

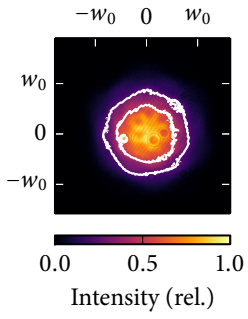

FIGURE 3.8: Photo of the far-field mode of the photonic crystal fiber after collimation. The white contour lines indicate the same intensity. A hexagonal pattern is visible in the intensity distribution. Here, w_0 refers to the $1/e^2$ beam radius of a two-dimensional Gaussian fit. Note that defects on the camera filter slightly distort the image and the contour lines.

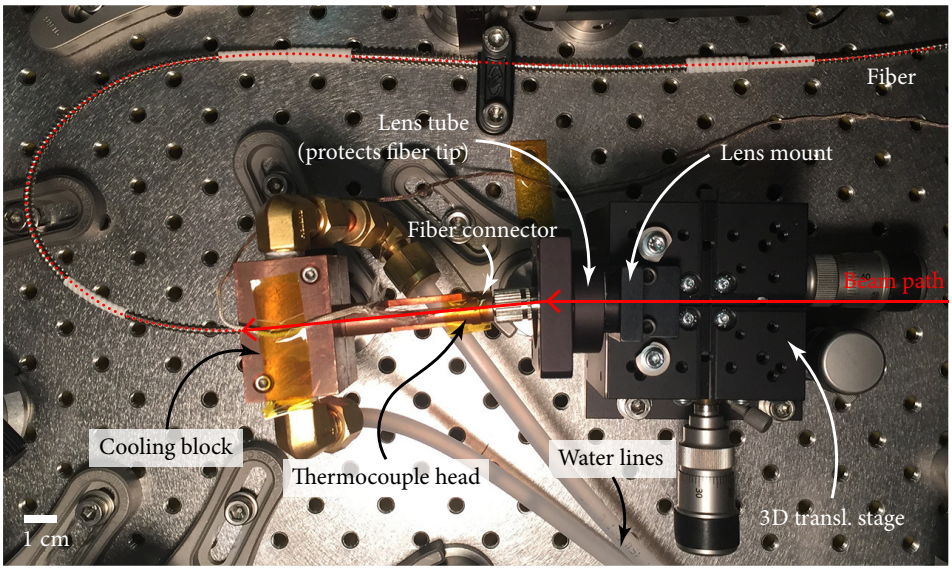

FIGURE 3.9: Photo of the high power photonic crystal fiber coupling setup with water cooling, thermocouple probe, and 3D translation stage. The thermocouple probe is connected to a read-out device. Note that the setup is nearly identical for all high power beam paths in the 1064 nm setup.

the fiber coupling efficiency[5]. Figure 3.9 shows the complete in-coupling setup for a single Holey fiber. When initially testing the maximum power handling capability of the fiber, the temperature was monitored continuously with an IR camera. Thermal images from the camera with no light and high power light present are shown in Figure 3.10. The maximum output power achieved is ≈ 18 W at 86 % fiber coupling efficiency without any AOMs in the beam path. Usually, the fiber coupling is adjusted continuously while ramping up the power to account for change in the AOM mode and thermal lensing of optics in the beam path. The lens used for fiber coupling

[5]The fiber coupling efficiency is mainly determined by the mode overlap. AOMs introduce ellipticity to the beam, which reduce the mode overlap.

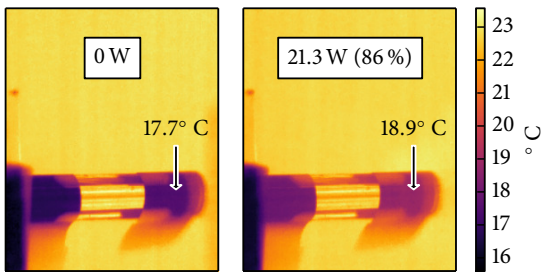

FIGURE 3.10: Thermal image of the input high-power fiber connector with (left) and without light (right). Three strips of Kepton tape are used to record the black body spectrum of the copper, which is otherwise highly reflective. The strips are located on the cooling block and the back as well as front of the copper ferrule (as shown Figure 3.9).

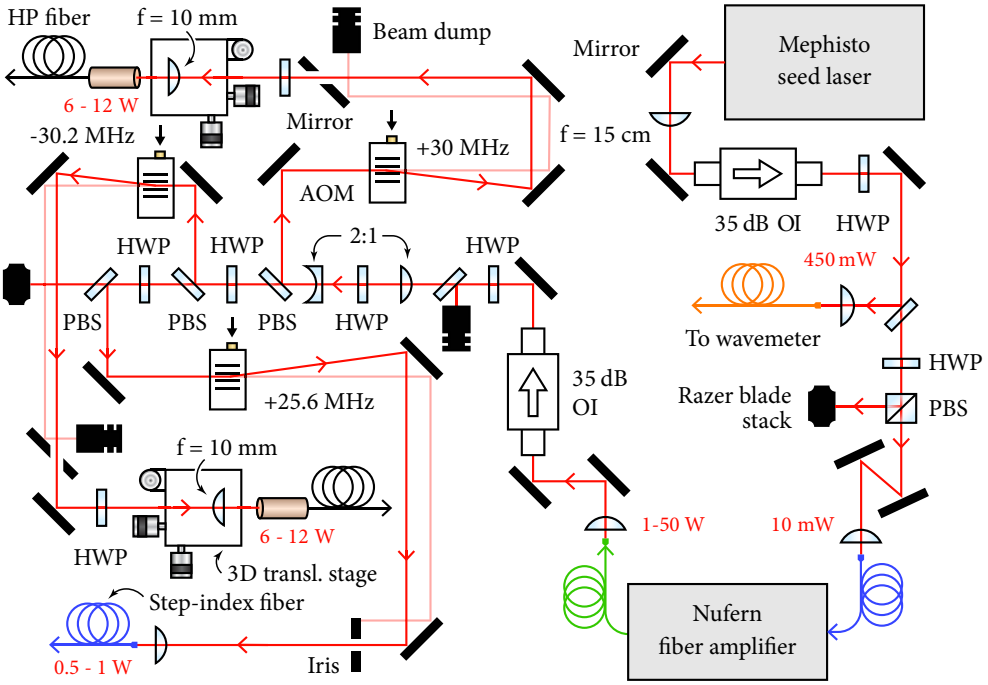

FIGURE 3.11: The complete 1064 nm laser setup. The beam path is shown in red with arrows indicating the propagation direction. Light red lines refer to the 0^{th} orders of AOMs. Laser power is denoted in red font. Coiled colored and black lines refer to optical fibers (green is unspecified, orange is multi-mode, blue is step-index, and black is Holey).

is mounted on a three-dimensional differential translation stage, which allows fine adjustment in all three directions.

C. THE COMPLETE 1064 NM LASER SETUP

The 1064 nm main setup is on a steel breadboard that sits on rubber spacers, which are on a floating table. This allows decoupling of vibrational noise from the table. Light from the main setup is delivered to the mezzanine with three fibers. The main setup consists of two parts: the seed laser optics and the fiber amplifier optics. We discuss those separately by following the beam path shown in Figure 3.11. Section 3.2 discusses the optics on the mezzanine.

The seed laser delivers 500 mW of 1064 nm light. A 35 dB (specified from manufacturer) fixed-wavelength isolator (Thorlabs IO-5-1064-VHP) is used to reduce the intensity of back-reflections. Approximately 90 % (measured) transmission can be achieved with maximized rejection. We use a half-waveplate and an AR-coated window to pick off $1 - 5$ % of the light, which is coupled into a multi-mode fiber going to the wavemeter. This allows to monitor the wavelength and detect potential multi-mode emission of the laser. A half-wave plate and a PBS cube allows us to

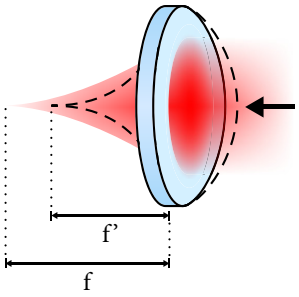

FIGURE 3.12: Thermal lensing of a convex lens: The transverse intensity distribution of laser beams (in general) is given by a Gaussian. Absorption of laser light by the optics leads to heating and expansion of the glass, but this expansion is non-uniform due to the Gaussian intensity distribution. Thus, the focal length ($f \rightarrow f'$) of the lens is decreased as a function of incident laser power. This introduces instability, especially for fiber coupling, which strongly depends on the beam $1/e^2$ radius

choose the amount of power, which is coupled into the fiber and the amount that goes into to fiber amplifier.

All optics after the fiber amplifier are exposed to high optical powers (30 – 40 W) at a relatively small $1/e^2$ beam radius (1.1 – 0.5 mm). Thus, thermal lensing is an issue – see Figure 3.12 for an illustration of the effect. Undesired reflections from surfaces are also more problematic for safety and stability at high power. We use high-power optics to minimize these effects:

- All transmissive optics are made from fused silica. Fused silica has better transmittance of 1064 nm light (i.e. less absorption) than BK7 and a lower coefficient of thermal expansion (5.5×10^{-7}/ °C compared to 7.1×10^{-6}/ °C) [19]. This reduces thermal lensing.
- All optics are V-coated with a narrow-band coating that is HR (mirrors) or AR (lenses) for 1064 nm. This minimizes undesired back-reflection from lenses and transmission of light through HR coated mirrors.
- Thin-film polarizing beam splitters (CVI TFPN-1064-PW-1025-UV) are used instead of regular polarizing beam splitter cubes. They use a coating to reflect s and transmit p-polarization. Regular PBS cubes are epoxied at the beam splitter interface. This can easily be damaged by high power laser beams.

The output fiber of the fiber amplifier is connected to a fixed collimator from Nufern yielding a collimated beam with a $1/e^2$ radius of approximately 1.1 mm.[6]. We use a 35 dB (specified from manufacturer) fixed-wavelength isolator (Thorlabs IO-5-1064-VHP) to protect the fiber amplifier from back-reflections. The isolator transmits 89 % (measured) of the light when rejection is maximized. The isolator uses two Brewster windows (polarization analyzers) at the input and output. This leads to non-normal output angles of the rejected light which escapes through windows. We

[6]The output fiber of the Nufern fiber amplifier has an unusual connector (LD-80 from Leonie Fiberoptics). We tried to use a custom collimator made from a solid piece of aluminum with a lens yielding a smaller collimated beam radius. However, it was not possible to get the fiber tip perfectly centered with respect to the lens which yielded an elliptical beam. This does not to seem to be a problem with the non-adjustable collimator made by Nufern.

use two custom-made beam dumps for safety and avoiding heating the breadboard. The beam dumps are made from aluminum that is sand-blasted and anodized in black to minimize potential reflection. Additionally, a v-groove in the beam dumps makes sure rejected light is trapped and cannot escape. Due to the relatively large thermal load of the beam dumps, their temperature increases only a few ˚C under load.

A HWP and a PBS directly after the optical isolator allow us to dump most of the power into the beam dump during initial alignment or for realignment. The mode of the fiber amplifier changes with the output power so that it is useful to always run it at full power and just drop most of the power directly after the optical isolator. We use a 2:1 ($f_1 = 200\,\text{mm}$ and $f_2 = -100\,\text{mm}$) telescope to reduce the $1/e^2$ beam radius since the 1.1 mm output beam from the Nufern collimator is too large for the active aperture of the AOMs[7]. After the telescope, the beam is split into three beams using three pairs of HWPs and PBSs. The first beam is for the horizontal optical dipole trap, the second beam is for the vertical optical dipole trap, and the third beam is for the dimple trap with relative low power (1 − 2 W) compared to the two other beams.

The optics for each beam path are identical, but the beam path for the dimple beam uses regular BK7 instead of fused silica optics. AOMs with a center frequency of 30 MHz (IntraAction AOM-30AF3) are used to control the intensity of the beams by controlling the amplitude of the RF signal driving the transducer in the AOM. We use the $\pm 1^{\text{st}}$ order and detune the AOM frequencies relative to each other to prevent undesired interference patterns at the atoms. The diffraction efficiency of the AOMs into the $\pm 1^{\text{st}}$ order is approximately 85 %. If we use the $\pm 1^{\text{st}}$ orders, then the 0^{th} and $\mp$1st orders still have significant power (15 % combined). For safety reasons we pick off the unused orders with a slitted mirror. A 3.5 mm slit is ground into the mirror allowing only one order to propagate straight while all other orders are reflected into a beam dump (see Figure 3.11). A HWP before the fiber coupling lens is used to align the polarization axis to the axis of the polarization-maintaining fiber. This reduces polarization fluctuations from acoustic and thermal noise. We use a V-coated fused silica lens ($f = 10\,\text{mm}$, Thorlabs LA4280-YAG) to focus the beam down onto the fiber tip. From Gaussian beam propagation (ABCD-matrices) we know that the $1/e^2$ radius w_f of the focused beam is given as $w_f = 2f\lambda_0/(\pi w_0)$. So for our configuration of $w_0 = 0.5\,\text{mm}$ $w_f = 6.8\,\mu\text{m}$, which is as close as we can get to the $1/e^2$ mode radius (6.3(0.75) µm [16]) of the photonic crystal fiber with commercially available lenses. The lens is glued into an adapter that is mounted inside a custom-made lens holder. The photonic crystal fiber and the coupling process are described in the previous section. The beam path for the dimple beam is identical (see Figure 3.11), but a regular polarization-maintaining step-index fiber (Thorlabs P1-1064PM-FC-5) is used.

The optics on the mezzanine are limited to collimation and shaping of the beam from

[7] The AOM still diffracts the beam, but the beam quality is degraded and the diffraction efficiency is reduced.

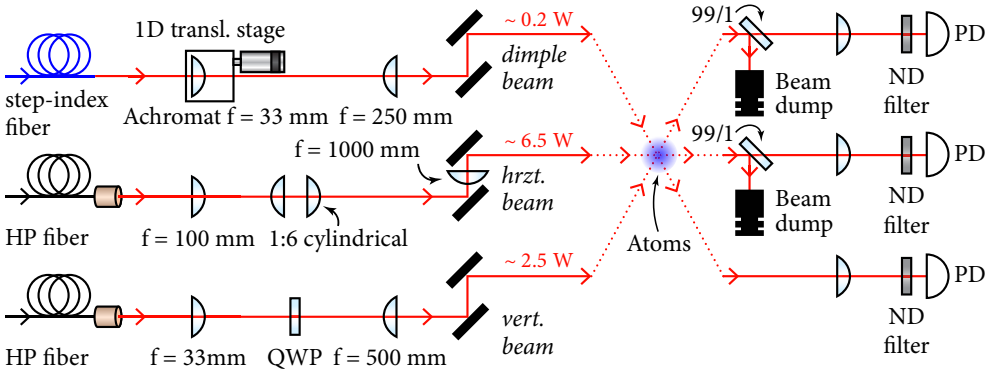

FIGURE 3.13: 1064 nm mezzanine optics for beam shaping of the three optical dipole trap beams and intensity stabilization. Two mirrors per beam path allow to fully control direction and angle of incidence at the atoms. Note that the beam paths are not in the same plane and the three beams hit the atoms at different angles (dotted lines). See Section 5.3 for a description of the different beam directions and angles.

the fiber to achieve the desired trap geometry. The optics are shown in Figure 3.13. The optics for each beam are nearly identical as follows

- Dimple dipole trap: We use a $f = 33$ mm achromat to collimate the beam and a $f = 250$ mm to focus the beam down to a $1/e^2$ radius of approximately 17 µm at the atoms. The Rayleigh length is relatively short (853 µm) for this beam and we use a 1D translation stage to adjust the focus of the beam.
- Horizontal dipole trap: We use a $f = 100$ mm lens to collimate the beam, a $f = 300$ mm and a $f = 50$ mm cylindrical lens to make the beam shape elliptical with a 6:1 horizontal to vertical ratio. A $f = 1000$ mm is used to focus the beam down to a $1/e^2$ radius of approximately 240 µm × 40 µm (horizontal × vertical) at the atoms.
- Vertical dipole trap: We use a $f = 33$ mm lens to collimate the beam and a $f = 500$ mm to focus the beam down to a $1/e^2$ radius of of approximately 106 µm at the atoms. A QWP before the atoms is used to circularly polarize the beam. This allows more efficient cooling into the optical dipole using the red MOT beams [20].

Optics for intensity stabilization are placed after the atoms on the mezzanine and shown in Figure 3.13. We use thin-plate 99:1 beam splitters to dump most of the high power light into beam dumps. The beam dumps are water cooled with a custom-made copper block to prevent heating of the mezzanine and drift of optics. The remaining power is focused onto photodetectors connected to the intensity servos. See Section 4.1 for a discussion of the intensity servo and its components.

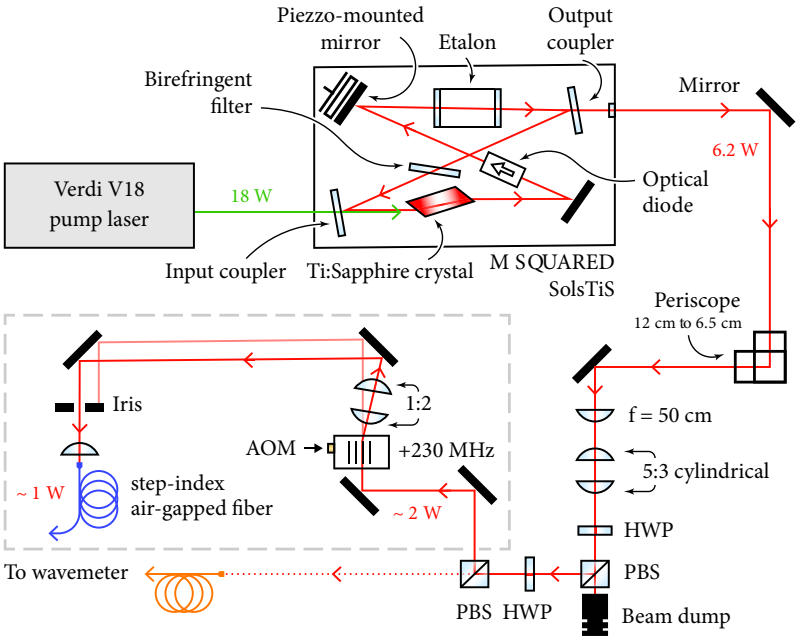

FIGURE 3.14: The 813 nm laser setup for one lattice beam; The beam path is shown in red (green: 532 nm pump) with arrows indicating the propagation direction. Light red lines refer to the 0^{th} order of an AOM. Laser power is denoted in red font. Coiled blue lines denote step-index fibers (orange: multi-mode fibers). The internal beam path and optical elements of the Ti:sapphire laser are shown on the top (from Ref. [21]). The elements surrounded by a dashed line will be duplicated for all three beams (indicated by the red dotted line). Note that the size of the SolsTiS laser is actually much smaller than the pump laser head.

In summary, the 1064 nm laser system is able to deliver a maximum total power of approximately 20 W at the atoms using Holey fibers. This makes our setup robust against pointing noise from the fiber amplifier and allows us to swap the fiber laser in an event of failure quickly without the need to realign the optics relative to the atoms.

3.3 THE 813 NM LASER SETUP

The 813 nm laser setup is not completed as of writing this thesis. However, a basic overview of the setup is given in this section since some work described in the Section 4.2 refers to the 813 nm laser setup. We limit the discussion to Figure 3.14, which shows the setup for a single beam path and the Ti:sapphire laser itself.

A. TI:SAPPHIRE LASER

We use a Ti:sapphire laser (M SQUARED SolsTiS) pumped by 18 W of 532 nm light (Coherent Verdi V18). The SolsTis laser features a sealed and alignment-free design that is supposed to deliver frequency stable light. However, first measurements showed drift of the output power, pointing noise, and frequency drift after a cold start. We therefore usually turn the laser on two hours before we intend to use it. The Ti:sapphire laser can be tuned by controlling the angle of a birefringent plate that introduces wavelength-dependent loss and by adjusting the length of an etalon in the beam path inside the bow-tie cavity (see Figure 3.14). The etalon can be locked using a dither lock, which stabilizes the (short-term) frequency of the laser. The maximum output of the Ti:sapphire laser at 813 nm is 6.2 W (with a single mirror in the beam path). The laser controller is connected via Ethernet and all settings of the laser can be directly controlled from a web browser on any computer in the lab. Additionally, the controller has a JSON (JavaScript Object Notation)[8] based interface that we use to lock the frequency.

[8] Data-interchange format and readily implemented in most modern programming languages.

4

EXPERIMENTAL TECHNIQUES

This section contains information on techniques employed in the experiment. We explain the intensity servo used for the 1064 nm (and 813 nm) laser system as well as the wavemeter based frequency servo for the 813 nm laser.

4.1 INTENSITY SERVO

The discussion in Section 2.3 showed that laser intensity noise leads to heating of atoms in optical dipole traps. We use a servo loop to suppress intensity noise. The details of the servo loop are discussed in this section. First, we are interested in fundamental limits of the minimum laser noise floor and explain the photon shot noise limit in Subsection A. This allows us to understand the design of the photodetector.

A. PHOTON SHOT NOISE AND THERMAL LIGHT SOURCES

First we establish a basic understanding of photon number fluctuation in an ideal light source. Assume we have a light source with constant intensity, i.e. constant power P. This light has a mean photon flux $\overline{n}$ of

$$\overline{n} = \frac{P}{\hbar\omega}. \tag{4.1}$$

Here ω is the angular frequency of the photons. The standard deviation is given as $\sqrt{\overline{n}}$, which we call photon shot noise [6, p. 778]. Furthermore, the signal-to-noise

ratio SNR is given as

$$\mathrm{SNR} = \frac{\overline{n}}{\sqrt{\overline{n}}} = \sqrt{\overline{n}} = \sqrt{\frac{P}{\hbar\omega}}. \tag{4.2}$$

The SNR is a function of the power P, so in general high signal-to-noise ratio can be achieved using high power. Quantum mechanics sets a fundamental limit on how little noise light can have. Most light sources, such as lasers, are coherent states, with a photon number noise set by $\sqrt{\overline{n}\tau}$ where τ is the averaging time. Photons from a coherent state follow Poissonian statistics described in the equations above. The SNR in Eqn. 4.2 is the theoretical limit on the performance of the intensity servo.

More interestingly, we can also show that photons from a thermal noise source can follow Poissonian statistics. This result allows us to easily measure photon shot noise with a photodetector. We know that the probability $p(n)$ for n photons at temperature T is given by the Bose-Einstein distribution [6, p. 466]

$$p(n) = \frac{1}{\overline{n}+1}\left(\frac{\overline{n}}{\overline{n}+1}\right)^n \tag{4.3}$$

with

$$\overline{n} = \frac{1}{\exp(\hbar\omega/k_\mathrm{B}T) - 1}. \tag{4.4}$$

The Bose-Einstein distribution has standard deviation $\sqrt{\overline{n}+\overline{n}^2}$ and thus is super-Poissonian. However, we have only considered one mode out of the quasi-continuum of thermal modes in the visible spectrum. Photodetectors can be broadband and detect a multitude of modes. Before we proceed, consider these two remarks from basic probability theory [22, p. 372]:

1. The Bose-Einstein distribution is a geometric distribution of the form $p(n) = (1-p)^n p$ for $(1-p) \equiv \overline{n}/(\overline{n}+1)$.

2. The distribution of a sum of N independent geometric distributions is a negative binomial distribution given as

$$p_N(n) = \binom{N+n-1}{n} p^n (1-p)^N = \frac{\Gamma(N+n)}{\Gamma(n+1)\Gamma(N)} p^n (1-p)^N. \tag{4.5}$$

   Here Γ is the Gamma-function with $\Gamma(n) \equiv (n-1)!$. The mean of the geometric distribution is given by $pN/(1-p)$. So for constant mean C (independent of N) $p = C/(N+C)$.

Back to physics – let $N = N_\mathrm{m}$ where N_m is the number of thermal modes and assume $N_\mathrm{m} \to \infty$, but while keeping the intensity and therefore the mean of $p_{N_\mathrm{m}}(n)$ is

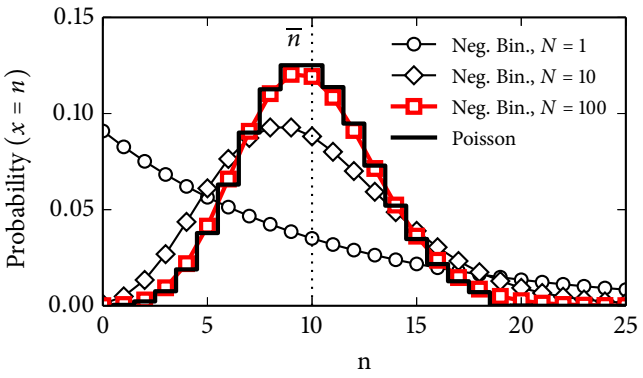

FIGURE 4.1: Poisson and negative binomial distributions for different N (see Eqn. 4.5) and constant mean $\overline{n}$. Note that for $N = 1$ the negative binomial distribution is equal to the Bose-Einstein distribution.

constant. We denote this average by $\overline{n}$. Then $p = \overline{n}/(\overline{n} + N_\mathrm{m})$ and we find

$$p_\infty(n) = \lim_{N_\mathrm{m}\to\infty} \frac{\overline{n}^n}{n!} \underbrace{\frac{\Gamma(N_\mathrm{m}+n)}{\Gamma(N_\mathrm{m})(N_m+\overline{n})^n}}_{\xrightarrow{N_\mathrm{m}\to\infty} 1} \underbrace{\left(\frac{1}{1+\overline{n}/N_\mathrm{m}}\right)^{N_\mathrm{m}}}_{\xrightarrow{N_\mathrm{m}\to\infty} \exp(-\overline{n})} = \frac{\overline{n}^n \exp(-\overline{n})}{n!}. \quad (4.6)$$

This is the Poisson distribution. See Figure 4.1 for a plot of the negative binomial distribution for different N_m compared to the Poisson distribution. If we consider many thermal modes, the light is Poissonian in the limit of infinitely many modes. This condition is usually fulfilled in the visible spectrum. Thus, a thermal light source is shot noise limited in terms of Eqn. 4.2 and is suitable for measuring photon shot noise for a given dc intensity.

B. PHOTODIODES

For detection of photons and measuring laser intensity a suitable detector is required. Semiconductor photodiodes work well for visible to near-infrared light. They have high quantum efficiency (~ 0.9) compared to photo multiplier tubes and high bandwidth (> 10 GHz) compared to thermal detectors. We are interested in two aspects of photodiodes: Signal-to-noise ratio and bandwidth. This section explains limitations of both.

Photodiodes consist of a *p-n junction*, which is an interface of a p-type (excess of holes) and a n-type (excess of electrons) semiconductor. At the interface electrons and holes can diffuse and the *depletion region* is formed. Photons that hit a p-n junction can create an electron-hole pair if their energy $\hbar\omega$ is larger than the band gap of the semiconductor used. Those electron-hole pairs contribute to a current that can be measured on the terminals of the p-n junction. This current is called *photo current*. The probability that a photon creates an electron-hole pair as a function of the photon wavelength λ is the *quantum efficiency* $0 \leq \eta(\lambda) \leq 1$ of the photodiode [6, p. 753]. The *responsitivity* $\Re = \eta\lambda/1.24$ is quantity that is defined in terms of η and λ.

TABLE 4.1: Performance figures of photodiodes from Hamamatsu used for intensity stabilization. All values are quoted from the manufacturer data sheet [25, 26].

			Operating conditions				
Model	Semiconductor	Diameter	Wavelength	Responsitivity	Bias volt.	Capacitance	Dark curr.
S3072	Silicon	⌀ 3 mm	813 nm	≈ 0.55 A/W	−12 V	≈ 8 pF	0.12 nA
G12180	InGaAs	⌀ 2 mm	1064 nm	≈ 0.59 A/W	−5 V	≈ 200 pF	2 nA

It is usually quoted in units A/W and allows direct calculation of the photo current from the incident light power. Silicon photodiodes are inefficient at wavelength $\gtrsim$ 1000 nm ($E(\gamma, 1000\,\text{nm}) = 1.23\,\text{eV}$) in terms of η and speed. The reason for this is that silicon (band gap ≈ 1.1 eV at 300 K [23]) is almost transparent for NIR photons. Thus, fewer photons are absorbed (smaller η) and the photons are absorbed outside the depletion region. Once the electron-hole pair is created outside the depletion region, it can take a substantial amount of time before they drift to the junction and contribute to the photocurrent. InGaAs (band gap ≈ 0.75 eV at 300 K [24]) photodiodes are a better choice for 1064 nm – our optical dipole trap wavelength ($E(\gamma, 1064\,\text{nm}) = 1.17\,\text{eV}$). Using Eqn. 4.2 and not considering internal sources[1] of noise, the SNR of the photodiode for a shot noise limited light source is just given as

$$\text{SNR}_{\text{PD}} = \sqrt{\eta \frac{P}{\hbar\omega}}. \tag{4.7}$$

So the SNR is reduced by $\sqrt{\eta}$ since only η photons out of a single photon contribute to the photo current. For a given wavelength we want to maximize $\eta(\lambda)$ and P to maximize the SNR. However, we can not measure arbitrarily large powers P due to the damage threshold of the semiconductor and the non-linearity of the p-n junction. Photodiodes generate a photocurrent proportional to the incident light power. We need to convert this current to a voltage that can be measured. The simplest current-to-voltage converter can be realized using a resistor R. If the resistor is connected to the two terminals of the photodiode we can measure the voltage $U_{\text{ph}} = RI_{\text{ph}} = R\eta P/\hbar\omega$. The resistor sets the gain, so for high gain a large resistance R is required. The bandwidth, which sets the maximum speed the voltage will respond to a change in light intensity, is then given by the RC-constant $f_{-3\,\text{dB}} \approx 1/2\pi RC_{\text{j}}$. Here C_{j} is the capacitance of the p-n junction, which basically acts as a parallel plate capacitor separated by the thickness of the depletion region. Usually C_{j} is lower for Silicon than InGaAs photodiodes and C_{j} increases with the active area for the same semiconductor. From electrostatics, the diode junction capacitance C_{j} is given

[1] Internal sources of noise are Johnson (thermal) noise from the shunt resistance of the diode and current shot noise from the dark current.

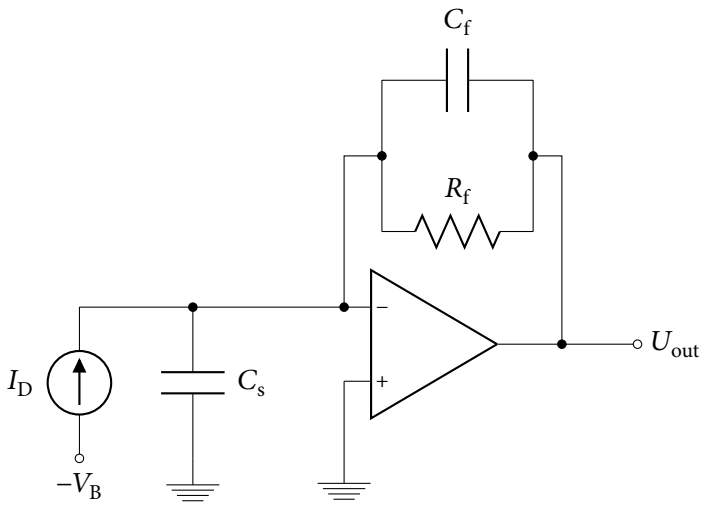

FIGURE 4.2: Simplified transimpedance amplifier circuit. The photodiode is shown with a simplified equivalend circuit: Current source I_D and capacitance C_s. Note that we can include differential and common-mode capacitance of the terminals of the operational amplifier in C_s since the positive terminal of the operational amplifier is connected to ground.

by [27]:

$$C_j^2 \propto \frac{1}{(\phi_i - U)}. \tag{4.8}$$

Thus, when we reverse bias photodiodes, i.e. $U < 0\,\mathrm{V}$, the capacitance is reduced, which is favorable for high speed applications. The decrease of the capacitance can be explained by considering that the depletion region thickness is increased under reverse bias voltage. Additionally, a reverse bias voltage also helps to operate the diode in the linear regime. However, the dark current increases as a function of reverse bias, which limits the minimum detectable light level. Table 4.1 lists the performance figures of the photodiodes used for intensity stabilization. We use $\varnothing$ 3 mm silicon photodiodes for intensity stabilization of the 813 nm laser for the optical lattice and $\varnothing$ 2 mm InGaAs photodiodes for intensity stabilization of the 1064 nm laser for the optical dipole trap. The large active area of the photodiodes allows us to be less sensitive to pointing noise.

C. LOW NOISE TRANSIMPEDANCE AMPLIFIER

Operational amplifier based transimpedance amplifiers (TIA) can be used to increase the bandwidth of photodiodes for a given gain and junction capacitance. This allows higher bandwidth than discussed in the last section. We discuss the principle of operation for these transimpedance amplifiers in this section.

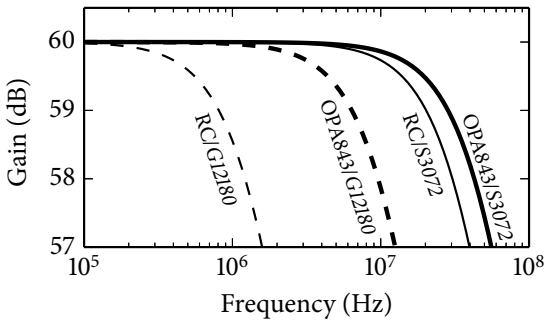

FIGURE 4.3: Bandwidth boost by using a transimpedance amplifier for the photodiodes used in the experiment. The frequency response for simple resistor (RC) and transimpedance (OPA843) current-to-voltage conversion is shown for the operational amplifier OPA843. Model numbers refer to the photodiodes in Table 4.1.

A simplified transimpedance circuit with a reverse-biased photodiode is shown in Figure 4.2. We know that the output voltage U_{out} of a non-ideal operational amplifier (gain $< \infty$) as a function of the inverting U_- and non-inverting U_+ input is given as [28, p. 233]

$$U_{\text{out}} = A(U_+ - U_-). \tag{4.9}$$

Here A is the open-loop gain of the amplifier. It approximately follows the frequency and phase response of a first-order low-pass filter [28, p. 191]

$$A(\omega) = \frac{A_{\text{DC}}}{1 + i\omega/\omega_c}. \tag{4.10}$$

Here A_{DC} is the open-loop gain at DC and ω_c is the frequency at which the gain is 3 dB lower than at DC. If we use Kirchhoff's current law to solve for U_{out} in Figure 4.2 we easily find

$$U_{\text{out}}(\omega) = \Re P \underbrace{\left\{ \frac{1 + i\omega C_{\text{f}} R_{\text{f}}}{R_{\text{f}}} \left(1 + \frac{1}{A(\omega)} \right) - \frac{i\omega C_{\text{s}}}{A(\omega)} \right\}^{-1}}_{\text{Gain as a function of the frequency } \omega}. \tag{4.11}$$

Here, $\Re$ is the responsitivity of the photodiode, P is the power of the light incident on the photodiode, and all other quantities are defined in Figure 4.2. The large open-loop gain $A(\omega)$ of the photodiode enhances the bandwidth of the photodetector as shown in Figure 4.3. The bandwidth, which is defined as the frequency of the -3 dB point of the gain, can be estimated as [29, p. 627]:

$$f_{-3\,\text{dB}} \approx \frac{\sqrt{f_{\text{RC}} f_{\text{GBP}}}}{2} = \sqrt{\frac{f_{\text{GBP}}}{8\pi R_{\text{f}} C_{\text{s}}}}. \tag{4.12}$$

Here, f_{RC} is the cutoff frequency defined by the feedback resistor R_{f} and the diode capacitance C_{j}. The gain-bandwidth product of the operational amplifier is given by f_{GBP}.

The feedback capacitor C_{f} is required to make the circuit stable. The optimal value

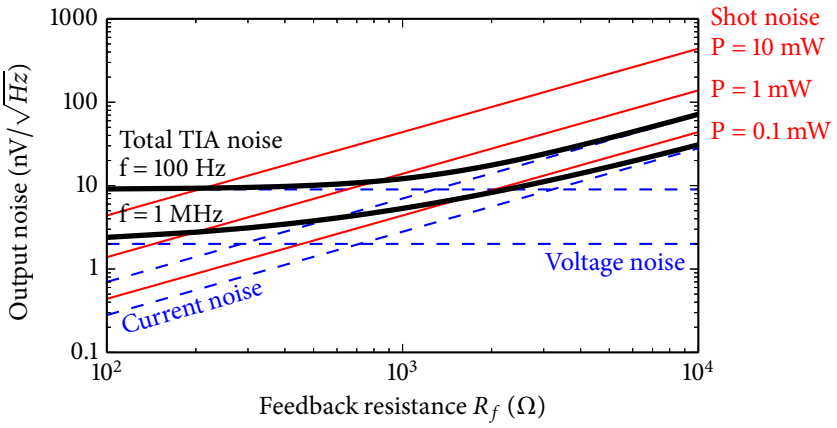

FIGURE 4.4: Output voltage noise from the operational amplifier OPA843 in the transimpedance circuit as a function of the feedback resistance R_f for two frequencies (100 Hz and 1 MHz). The photon shot noise is calculated for quantum efficiency $\eta = 0.6$. The region where the detector is shot noise limited can be estimated from this plot. All values are calculated from the specifications given in the manufacturer data sheet [30].

is given by $1/2\pi R_\mathrm{f}\sqrt{f_\mathrm{GBP} f_\mathrm{RC}}$ [29, p. 628]. However, stray capacitances present on printed circuit boards usually require an experimental selection of the exact value. This can be done by increasing the size of the capacitor until the output of the TIA stops ringing and then using a slightly larger capacitance to compensate for possible variations in component specifications.

We found the three key factors that determine the maximum bandwidth for a fixed transimpedance gain R_f:

- Source capacitance (C_s)
- Feedback capacitance (C_f)
- Gain-bandwidth product of the operational amplifier (f_GBP).

Table 4.2 lists performance figures for the operational amplifiers used for the TIAs.

Increasing the bandwidth of photodetectors using an operational amplifier is great - but there is no free lunch. Like most other electronic devices, operational amplifiers introduce noise. Using Kirchhoff's circuit laws, assuming that all noise is uncorrelated and that the shunt resistance of the photodiode R_shunt is much larger[2] than the feedback resistance R_f, the total mean-squared noise of the TIA u_N in units of

[2] This is a valid assumption for moderate gain.

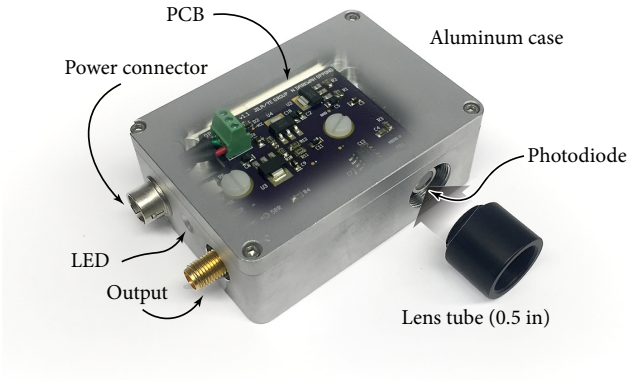

FIGURE 4.5: Photo of the photodetector with the different features. The lid of the aluminum case is shown as half transparent to reveal the PCB inside the case. The case measures 6.9 cm × 4.9 cm × 2.54 cm.

$\mathrm{nV}/\sqrt{\mathrm{Hz}}$ is given as [31]

$$u_{\mathrm{N}} = \sqrt{\left(\underbrace{2ei_{\mathrm{dark}}}_{\text{(i)}} + \underbrace{\frac{4k_{\mathrm{B}}T}{R_{\mathrm{shunt}}}}_{\text{(ii)}} + \underbrace{i_N^2}_{\text{(iii)}} + \underbrace{\frac{4k_{\mathrm{B}}T}{R_{\mathrm{f}}}}_{\text{(iv)}} \right) R_f^2 + \underbrace{e_N^2}_{\text{(v)}} \left(1 + \frac{R_{\mathrm{f}}}{R_{\mathrm{shunt}}} \right)^2}. \tag{4.13}$$

The different noise terms are the following:

(i) Current shot noise of the dark current i_{dark}

(ii) Johnson noise of the shunt resistance R_{shunt}

(iii) Current noise of the operational amplifier i_{N}

(iv) Johnson noise of the feedback resistor R_{f} at temperatue T (= 300K)

(v) Voltage noise of the operational amplifier e_{N} .

Note that in general the noise is white, i.e. flat across all frequencies. However, most operational amplifiers have $1/f$ voltage and current noise, which introduce a frequency dependence of Eq. 4.13. Field-effect transistor (FET) based operational amplifiers usually have higher voltage noise but lower current noise whereas the opposite applies to bipolar operational amplifiers. The output voltage noise depends on the voltage noise of the operational amplifier plus the current noise multiplied by the gain R_{f}. Thus, a rule of thumb is that for low gain bipolar and for high gain FET operational amplifiers yield the lowest overall noise. Since the available power for the intensity servo is large, we do not require high gain and choose a bipolar operational amplifier. Figure 4.4 shows total noise and the different contributions for the TIA used for the photodetectors. To fully characterize and control the amplitude noise of the light, the circuit's electronic noise floor must be below the photon shot noise. Additionally, we are ultimately limited by the photon shot noise of a constant intensity

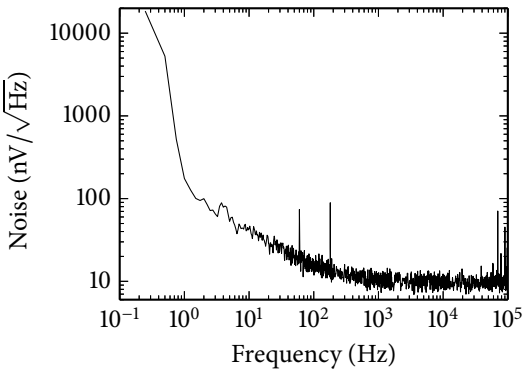

FIGURE 4.6: PSD of the TIA noise (without photocurrent) using the operational amplifier OPA843. At ≈ 200 Hz the noise level reaches the noise floor of 10 nV/$\sqrt{\text{Hz}}$. This agrees well with the calculated values. The noise peaks at 60 Hz and 180 Hz are due to noise on the power supply. The origin of the noise peaks at ≥ 40 kHz are unknown but seem to be electronic pickup from sources in the lab since they are not present in the spectrum for measurements at another location.

light source. If the noise floor of our photodetector is below the amplified shot noise for a specific light power P_0 we call it shot noise limited for P_0. When measuring intensity noise we have to make sure that we are actually measuring laser noise and not detector noise. For verification we could measure the noise of the photodetector while blocking light to see the dark response. However, if the frequency response of our detector has unusual resonances, we would not be able to see them in the dark response. We can use a result from the previous section and measure the intensity noise of a thermal light source. The detector is not mode selective and therefore the thermal light is Poissonian. We choose the power of the thermal light source such that the detector gives the same dc value as for the actual laser intensity noise measurement. The shot noise of the light is amplified by the transimpedance gain R_f. Thus, the expected PSD of the shot noise has a value of $\sqrt{2eU/R_\text{f}}$ (in units of V/$\sqrt{\text{Hz}}$) where e is the charge of the electron and U the measured dc voltage. We can then compare the thermal intensity noise level to the noise floor of the dark response and evaluate whether the detector is shot noise limited or not. We perform this measurements for all photodetectors used in the experiment. If the detector is not shot noise limited for a given power P_0 we increase the power until the detector is shot noise limited.

We are using the operational amplifier OPA843 from TI as the TIA in the photodetec-

TABLE 4.2: Performance figures for the operational amplifiers (OPA843) and TIA used for intensity stabilization. The photodiodes are those described in Table 4.1. All values are quoted from the manufacturer datasheet [30].

				Calc. TIA bandwidth for 1 kΩ	
Model	GBP	Voltage noise (freq.)	Current noise (freq.)	S3072 - Si	G12180 - InGaAs
TI OPA843	800 MHz	9 nV/$\sqrt{\text{Hz}}$ (100 Hz)	7 pA/$\sqrt{\text{Hz}}$ (100 Hz)	55.0 MHz	12.2 MHz

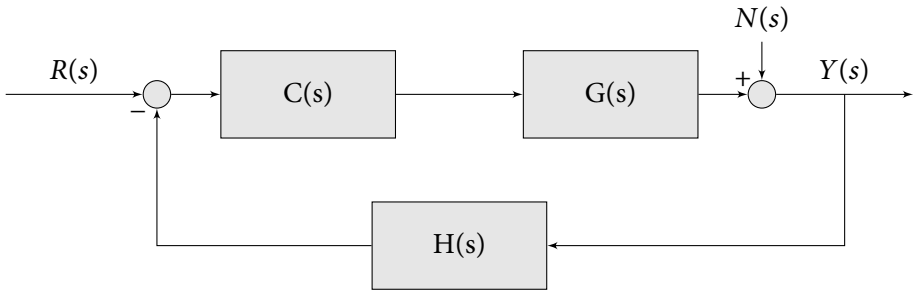

FIGURE 4.7: Closed servo loop with negative feedback. The quantities are given as: input $R(S)$, system $G(S)$, noise $N(S)$, loop filter/controller $C(s)$, feedback fraction $H(s)$, and output $Y(s)$.

tors. It offers a pretty large gain-bandwidth product of 800MHz while offering good dc performance in terms of noise (9 nV/$\sqrt{\text{Hz}}$ at 100 Hz). This is useful, since we use large area photodiodes (i.e. large junction capacitance) to reduce sensibility to pointing noise and make the setup more robust, i.e. not requiring frequent realignment of optics. The performance figures for both operational amplifiers and the resulting TIA can be found in Table 4.2. The TIA circuit used for detection of intensity noise is similiar to the basic circuit depicted in Figure 4.2. The full circuit for the TIA used for detection of intensity noise can be found in the Appendix. Additionally, variable regulators allow selection of the reverse biasing voltage by just two resistors. We use the OPA843 with an unbalanced power supply to increase the maximum positive voltage swing of the $\pm 5V$ supply operational amplifier. The PCB is designed with a 50 Ω transmission line (coplanar) on the output of the TIA to allow interfacing with 50 Ω systems, e.g. RF mixers. A solid aluminium case is used to shield the electronics from RF and other noise sources present in the laboratory. The case is a custom design to fullfill the strict space requirements on the optical table. It features a LED power indicator and a Hirose power connector that matches the standard power cable used in the lab. All connectors are on the top of the case to prevent cables from blocking optical beam paths. The aperture for the photodiode is tapped (0.535 inch) to allow attachment of Thorlabs 0.5 inch lens tubes. This allows to easily block background radiation and adding or swapping of neutral density filters. The case is made from two pieces of solid block aluminium machined on a CNC mill. Figure 4.5 shows a photo of the full assembly.

D. ANALOG SERVO LOOP

We measure the PSD of the intensity noise to calculate the resulting heating rate as a function of trapping frequency. The laser light is focused onto a low-noise

photodetector and the spectrum is recorded with a FFT machine[3], which fourier transforms the time domain signal. Figure 4.9 shows the basic measurement setup and Figure 4.10 the results for the 1064 nm laser system.

We use an analog servo loop to reduce laser intensity noise. This is necessary to minimize heating as described in Section 2.3. We use the JILA intensity servo, which has been developed by the electronics shop at JILA. First, we discuss how this loop filter works. Secondly, we explain the intensity stabilization setup and report the performance.

We use the Laplace transform to understand the behavior of a basic closed loop time-invariant system. This allows us to evaluate the JILA AOM intensity servo loop filter. The Laplace transform of a basic closed loop system is shown in Figure 4.7. Simple algebra yields the following expression for the output $Y(s)$

$$Y(s) = \frac{C(s)G(s)R(s)}{1 + G(s)C(s)H(s)} + \frac{N(s)}{1 + G(s)C(s)H(s)}. \tag{4.14}$$

Here all quantities are defined in Figure 4.7. Note that $s = i\omega$ where ω is an angular frequency. We find two conditions:

- For large $G(s)C(s)H(s)$ the noise $N(s)$ can be suppressed significantly on the output $Y(s)$, i.e. in general we want $G(s)C(s)H(s) \gg 1$ – especially at frequencies to which the atoms are sensitive, i.e. at twice the trapping frequency[4].
- For $G(s)C(s)H(s) = -1$ the output is unbound, i.e. the system becomes unstable. Thus, $|G(s)C(s)H(s)| \ll 1$ or $|G(s)C(s)H(s)| \gg 1$ if $\arg\{G(s)C(s)H(s)\} = \pi$.

Controlling the laser intensity requires introducing a nonlinear acousto-optical or electro-optical component. We use an acousto-optical modulator (AOM) to control the laser light intensity. The AOM is a delay limited system and we discuss the influence on stability of the servo loop here. A piezo-electric transducer drives a sound wave in the AOM crystal. This generates a modulation of the index of refraction in the crystal as a function of the sound wave intensity. The laser beam enters the crystal perpendicular to the sound wave and is diffracted into multiple orders. This effect is similar to diffraction on a grating[5]. The intensity of the sound wave determines the intensity of the different orders relative to the undiffracted (0^{th})

[3] FFT machines are real-time spectrum analyzers that have no lag due to a frequency sweep. This allows to observe dynamics in the frequency space. However, we are only using the FFT machine here because it is available in the lab and has low noise close to dc (1 Hz) and hight resolution (800 FFT points).

[4] Note that the noise cannot be suppressed below the noise floor of our detector. We might see that on an in-loop detector but an out-of-loop detector will show the absolute/real noise suppression.

[5] Note that the light is frequency shifted since the diffraction occurs on a moving and not a stationary modulation in the refractive index [6].

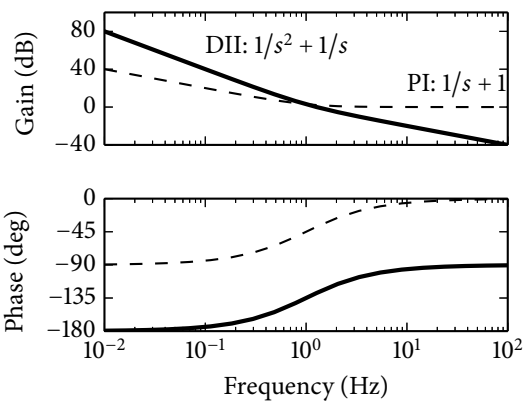

FIGURE 4.8: Bode plots of open-loop transfer functions for the double integrator plus single integrator (DII, thick line) and proportional plus integrator (PI, thin dashed line). The DII has a gain boost close to DC and compared to the PI. The -180° phase shift of the DII close to DC does not cause instability since the gain is much larger than one. Note that the frequency and gain scale is arbitrary and does not reflect the values in our setup.

order. Thus, we can modulate the intensity by changing the RF drive power. The AOM has two speed limitations, which are given as function of the speed of sound in the crystal v_s:

- The sound wave has to travel from the transducer to the position of the beam, the delay as a function of the distance d is given as $\tau = d/v_s$.
- The sound wave has to propagate through the non vanishing beam waist (assuming a Gaussian laser beam), the rise time as function of the $1/e^2$ beam radius w is given as $\tau = \alpha w/v_s$. Here α is a constant that is defined based on the definition of the rise time (i.e. from 10 % to 90 %).

If the RF drive power is changed, there will be a finite time delay until we see a change of the intensity distribution across the diffracted orders.[6] This time delay limits the servo loop, since it takes a duration of τ to write a correction onto the laser light. The time delay can be described by a phase shift of $-\omega\tau$ where ω is the frequency of interest. If this phase shift equals π the feedback becomes positive and the system unstable. We cannot compensate for this phase shift since the AOM introduces a time delay, which would require us to predict the intensity noise at a point in the future in order to write the correction onto the driving RF signal ahead of time. This is fundamentally different from a pure (constant) phase shift that is introduced by e.g. an integrator. For most systems the gain is below 1 before the time delay phase shift is π. However, AOMs have a relatively flat gain across a wide bandwidth, which is mainly determined by the bandwidth of resonance circuit driving the transducer. Thus, the gain does not roll off before the time delay phase shift is π. We need an integrator (K/s) in the loop filter $C(s)$ to make sure the gain is below 1 at this point. This system can then be controlled by a PI-controller, which results in a controller

[6] Note that the speed of light is much larger than the speed of sound, which is $\approx$ 3000 m/s for the AOMs used in the experiment. Thus, the delay is solely determined by the AOM

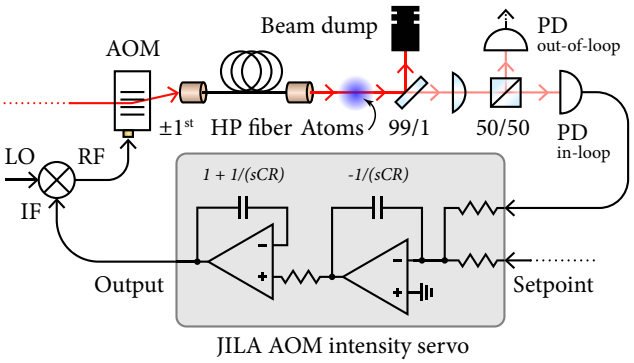

FIGURE 4.9: The intensity servo setup; the JILA AOM intensity servo (loop filter) is shown in the gray box (simplified), where the transfer functions of the two operational amplifier circuits are shown above.

with a double integrator and a single integrator:

$$C(s) = \frac{K_{ii}}{s^2} + \frac{K_i}{s} \tag{4.15}$$

Here K_{ii}, K_i are constants. This is how the JILA AOM intensity servo loop filter works. It allows higher gain close DC compared to a pure PI-controller as you can see in the Bode plots in Figure 4.8).

Figure 4.9 shows the setup we use to cancel intensity noise and also measure the performance of our servo loop. The overall intensity is controlled with an AOM and the $\pm 1^{st}$ order is coupled into an optical fiber that delivers the light to the atoms. We use a 99/1 beam splitter to dump most of the power into a beam dump. The remaining power is then split and focused onto two photodetectors. One of them is connected to the intensity servo (in-loop) and one is used to measure the performance of the servo (out-of-loop). The signal of the in-loop photodetector can be teed off and also be measured on the FFT machine. The output of the intensity servo is fed into the IF port of an mixer, which controls the LO/RF port isolation and thereby allows to control the RF power level that drives the AOM. The intensity servo setpoint is controlled by a voltage from the DAC board that runs the experimental sequence. This allows to ramp the intensity up or down in an arbitrary way.

Figure 4.10 shows the performance of the intensity servo for the 1064 nm. The overall

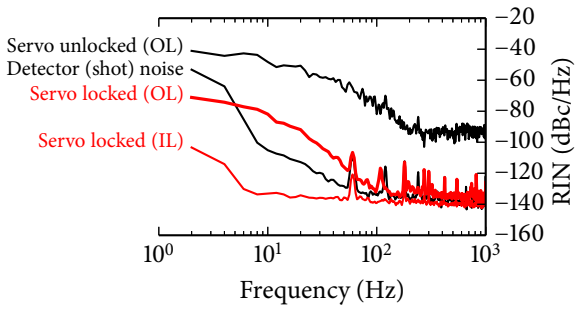

FIGURE 4.10: Intensity servo performance for 1064 nm laser system. The detector shot noise is measured with a thermal light source yielding the same dc light level. (OL) = out-of-loop and (IL) = in-loop.

noise beyond 100 Hz is reduced to −140 dB, which is close to the shot noise limit of the laser light. Shortcomings of our current intensity servo are that the response of the mixer is not linear, i.e. over a wide range of setpoint voltages it would be advantageous to linearize the mixer behaviour. This could be done using a digital instead of an analog loop filter. Further improvements include adding feed-forward during intensity ramps to decrease the error signal and improve the settling time.

4.2 FREQUENCY SERVO

The 813 nm laser we are using for the optical lattice has frequency drift on long timescales (see Figure 4.12) even when locked using the built-in etalon dither lock[7]. This introduces two potential problems:

- The magic wavelength condition is not fulfilled anymore and a differential ac Stark shift is introduced. This is especially a problem for high precision, i.e. clock measurements.
- All three lattice beams are retro-reflected and the mirrors define a fixed node of the electro-magnetic wave. Thus, when the wavelength changes, not only the spacing of the atoms is modulated but also the trap position. This can introduce heating as discussed in Section 2.3.

This is the motivation for building a simple frequency servo for the 813 nm laser. Luckily, the 813 nm laser offers an all digital interface, which allows changing the piezo voltage on one of the mirrors in the ring cavity. We can use a wavemeter that is regularly calibrated to the clock laser at 698 nm (stability of 10^{-16} at 1 s [2]) as a frequency standard. This should in principle allow to transfer the stability of the clock laser to the 813 nm laser. This section establishes a basic understanding of discrete PID controllers, explain the implementation in our setup, and the resulting performance of the servo.

A. DISCRETE PID CONTROLLER

Continuous linear time invariant systems are usually analyzed using the Laplace transform of the transfer function. This allows to evaluate transfer function of combined systems and stability criteria easily. However, digital controllers operate

[7] We do not now the exact way the dither lock is implemented in the M SQUARED SolsTiS laser. However, we can describe the general operating principle of a dither lock: the laser frequency is modulated with frequency Ω when the dither lock is engaged. The etalon transmission is measured and a lock-in amplifier with frequency Ω produces an error signal that is proportional to the offset from the etalon resonance. This error signal can be used to feed back onto the laser frequency using a mirror mounted on a piezo.

on discrete and not continuous space. This section discusses a method to derive a discrete transfer function from a continuous transfer function. Specifically, we are transforming the continuous transfer function of the PID controller.

The transfer function $C_{\mathrm{PID}}(s)$ of the continuous PID controller in s-space is given as [32]

$$C_{\mathrm{PID}}(S) = K_{\mathrm{p}} + \frac{K_{\mathrm{i}}}{s} + K_{\mathrm{d}} s. \tag{4.16}$$

Here, K_{p}, K_{i}, K_{d} is the proportional, integral, and derivative gain. We use the z-transform to discretize this controller, which is given as [32, p. 194]

$$s \leftarrow \frac{2}{T}\frac{z-1}{z+1}. \tag{4.17}$$

Here, T is the time step in the discrete system. Thus, we can obtain a transfer function in z space by replacing s with the expression in Eqn. 4.17. A full derivation of the z-transform is not given here but a very instructional derivation can be found in [33]. The z-transform takes a function from complex s-space to the (discrete) z-space, which is given by the unit circle in $\mathbb{C}$ [33, p. 561]. We can then express the transfer function in terms of a recursive function on discrete time space that can be easily implemented in a computer program or hardware logic, i.e. FPGAs. It is useful to bring the transfer function $H[z]$ in z-space to a general form[33, p. 563], which allows straight forward definition of the recursive function $y[n]$ on discrete time space. If the form of $H[z]$ is given as

$$H[z] = \frac{a_0 + \sum_{i=1}^{N} a_i z^{-i}}{1 - \sum_{i=1}^{N} b_i z^{-i}}. \tag{4.18}$$

Then $y[n]$ is simply given as

$$y[n] = \left(\sum_{i=0}^{N} a_i x[n-i]\right) + \left(\sum_{i=0}^{N} b_i y[n-i]\right). \tag{4.19}$$

Here, $y[n]$ is the output of the system and $x[n]$ is the input of the system as shown in Figure 4.11. Thus, for the continuous PID controller in Eq. 4.16 we find (after some tedious calculations)

$$H[z] = \frac{a_0 + a_1 z^{-1} + a_2 z^{-2}}{1 - b_2 z^{-2}}. \tag{4.20}$$

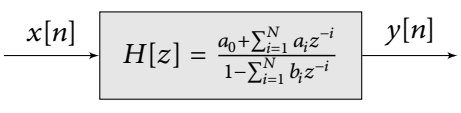

FIGURE 4.11: Discrete transfer function $H[z]$ on z-space. The input and output are given by $x[n]$ and $y[n]$, both are discrete time series.

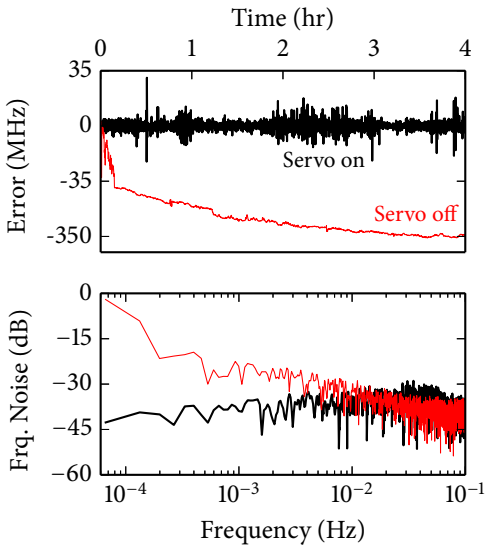

FIGURE 4.12: Wavemeter lock error signal in time space (top) and frequency space (bottom). The thick black trace shows the in-loop error signal with PID feedback every $T = 5$ s enabled. The red trace shows the error signal of the unlocked laser. Both data traces were taken one hour after a cold start of the laser. Note that the y-axis in the plot on the top has piece-wise linear scale from 35 to −35 MHz and from −35 to −350 MHz. The error signal in frequency space (bottom) is normalized to the maximum amplitude in the spectrum of the unlocked signal.

And thus the recursive function $y[n]$ is given as

$$y[n] = a_0 x[n] + a_1 x[n-1] + a_2 x[n-2] + b_2 y[n-2]. \tag{4.21}$$

The coefficients in terms of the proportional, integral, and derivative gain as well as the discrete time step T are given as

$$\begin{aligned} a_0 &= K_p + K_i \frac{T}{2} + K_d \frac{2}{T} \\ a_1 &= K_i T - K_d \frac{4}{T} \\ a_2 &= K_i \frac{T}{2} - K_p + K_d \frac{2}{T} \\ b_2 &= 1. \end{aligned} \tag{4.22}$$

So all we need to implement is simple multiplication with constants given by Eqn. 4.22, and two FIFO buffers, which each can store two values (either floating or fixed point numbers of the desired precision).

It is important to note that although the number of poles and zeros of the transfer function are not changed with the z-transform, their position in frequency space changes. This effect is called frequency warp and can be compensated for if an exact transform from s to z-space is required (e.g. for digital filter design). However, we are tuning the PID controller directly in the discrete form and therefore do not need to compensate for frequency warp.

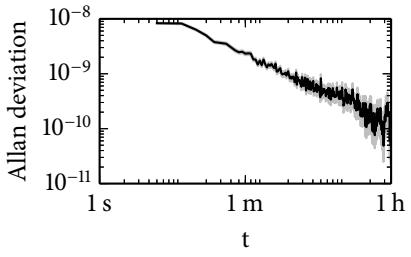

FIGURE 4.13: Allan deviation for the 813 nm laser with the digital PID lock engaged. The gray area denotes the statistical error. Note that this is the in-loop error signal and does not include drift of the wavemeter.

B. COMPUTER-BASED FREQUENCY SERVO

The laser for the 813 nm optical lattice features a network interface. This allows us to design an all digital feedback controller running on the computer that is connected to the wavemeter. For a description of the 813 nm laser system refer to Section 3.3.

We implement the digital PID controller as a class in the programming language Python (see Appendix for source code) and use a simple GUI to tune and monitor the PID controller. Additionally an interface to the 813 nm laser and the wavemeter control software[8] is implemented in a simple wrapper class. Thus we have a detector (wavemeter), actuator (piezo/laser network interface), and a loop filter (digital PID controller). This is a full laser frequency servo when combined. The GUI allows to select different channels of the multiplexed wavemeter as well as entering the network configuration for the 813 nm laser. The other Strontium experiment at Ye labs can potentially use the same program to lock their 813 nm laser simultaneously. The maximum rate of feedback is mainly limited by the network interface of the laser, which - even with an established connection - takes between 300 ms and 500 ms to complete a request. The sample respectively feedback rate can be controlled from the GUI.

The 813 nm laser has relatively large drift (compare with Figure 4.12) after turning on. The servo is able to suppress these fluctuations by as much as 40 dB. The servo allows the laser to reach a long term stability of 10^{-10} at one hour in terms of the Allan deviation (see Figure 4.13). Note that this stability is only relative to the detector and does not consider drift of the wavemeter.

[8] The wavemeter manufacturer offers a proprietary DLL that can be addressed using python ctypes. The library uses shared memory to exchange information with third-party tools. This is extremely useful as it allows real-time access to the current value with higher precision than the wavemeter software.

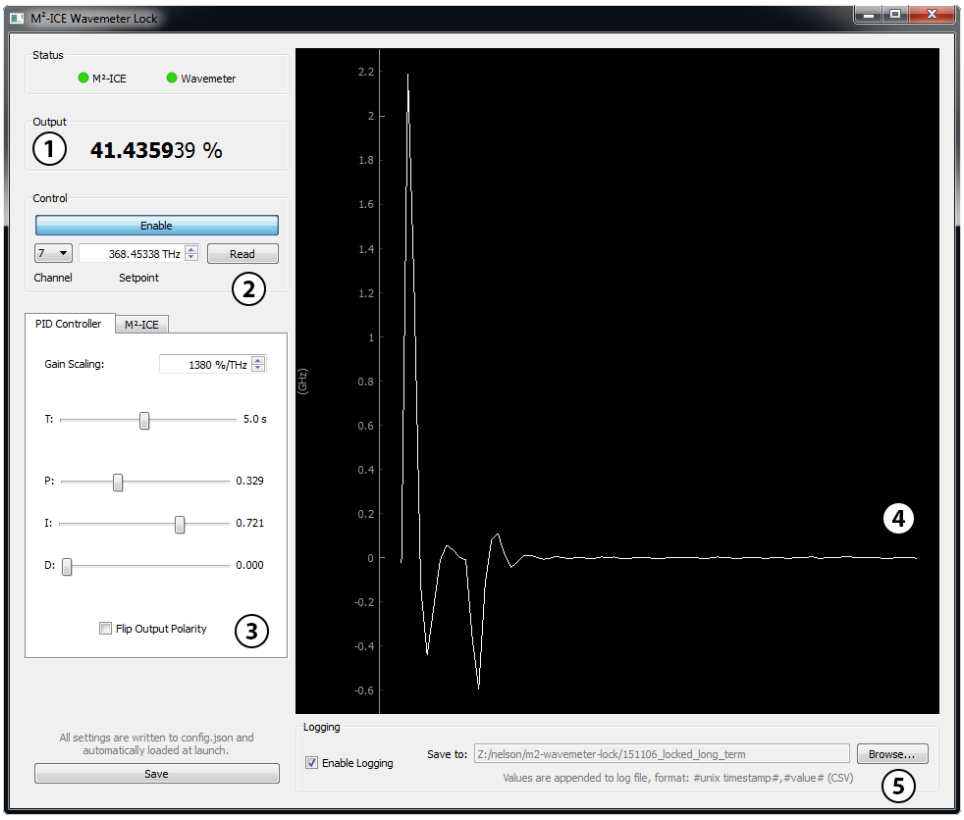

FIGURE 4.14: Wavemeter PID controller interface running on Windows 7. The numbers correspond to (1) current value written to the piezo voltage of the 813 nm laser, (2) wavemeter channel selection, setpoint, and enable/disable button, (3) PID parameters and sampling interval, (4) plot of the error signal as a function of time steps, and (5) logging feature.

5

TOWARDS QUANTUM DEGENERACY

This chapter discusses the elements of a typical experimental sequence, and summarizes the preliminary results from the first attempts of evaporatively cooling of strontium-87 in out crossed optical dipole trap. First, we explain the energy level structure of strontium-87 and discuss the blue and red MOT, which set the initial conditions for the evaporative cooling. Second, we explain the optical dipole trap geometry and show results from evaporative cooling in this trap. Last, results from this thesis are reviewed and an outlook is given.

5.1 ENERGY LEVEL STRUCTURE OF STRONTIUM-87

We give a short overview on the properties of strontium-87 that are necessary to understand the blue and red MOT described in the next section. Strontium is an alkaline-earth element, so there are two electrons in the outer electron shell. Thus, the atomic energy structure is split into a singlet ($\sqrt{1/2}\{|\uparrow\downarrow\rangle - |\downarrow\uparrow\rangle\}$) and triplet manifold ($|\uparrow\uparrow\rangle$, $|\downarrow\downarrow\rangle$, $\sqrt{1/2}\{|\uparrow\downarrow\rangle + |\downarrow\uparrow\rangle\}$). Transitions within the singlet or triplet manifolds are dipole-allowed and strong but transitions between manifolds are dipole-forbidden. Weak transitions with narrow linewidths are still allowed due to mixing of the singlet and triplet states. In particular, we use the weak transitions between the $^1S_0$ ground state and ^3P_J states for improved cooling and precision spectroscopy. The clock transition is the doubly-forbidden transition between the $^1S_0$ ground state and the $^3P_0$ excited state (698 nm) and has a linewidth of 1 mHz [35]. All relevant energy levels and transitions are shown in Figure 5.1. The nuclear spin of strontium-87 is 9/2. The spin of the ground state is purely nuclear and the resulting nuclear spin states are given as $m_F = -9/2, -7/2, \ldots, 7/2, 9/2$. The ten nuclear spin states can for example enhance s-wave scattering, which can be useful for efficient evaporative cooling in an optical dipole trap.

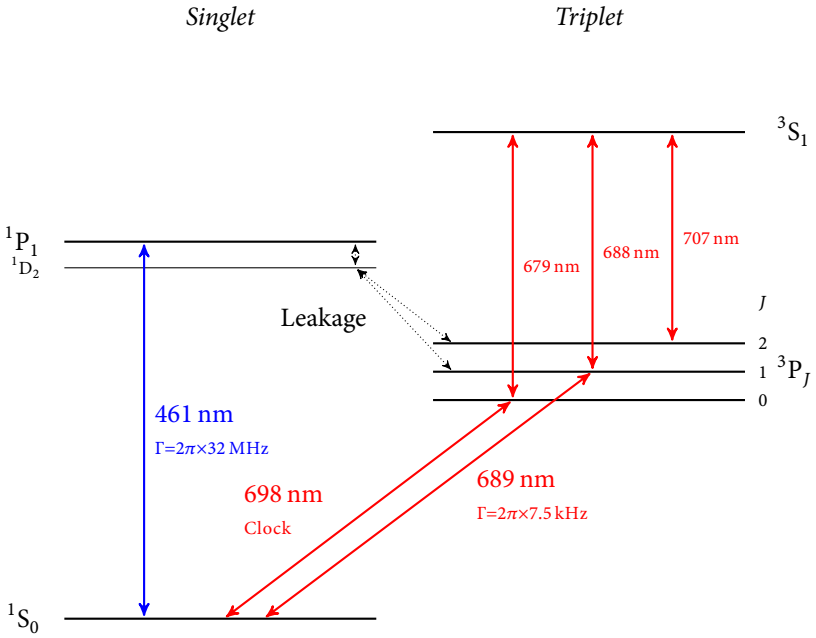

FIGURE 5.1: Energy level diagram for strontium-87 showing relevant singlet and triplet manifolds in the spectroscopic notation $\left({}^{2S+1}L_J\right)$. Level spacing values and transition linewidths are from Ref. [34]. Note that all level spacings are to scale except the ${}^3P_J$ spacings.

5.2 THE BLUE AND RED MOT

We use a three-dimensional MOT to capture, cool, and spatially confine the atoms in three dimensions.
Before the MOTs are described in detail, consider the theoretical limits for the minimum temperature achievable in a MOT [36, 37]:

$$T_{\text{Doppler}} = \frac{\hbar\Gamma}{2k_{\text{B}}} \qquad \text{(Doppler limit)}$$

$$T_{\text{recoil}} = \frac{h^2}{2Mk_{\text{B}}\lambda^2}. \qquad \text{(Recoil limit)}$$

Here Γ is the linewidth and λ is the wavelength of the cooling transition. M is the mass of a single strontium-87 atom. The Doppler limit is proportional to the linewidth of the transition. Thus, we expect lower temperatures for transition that are narrow. However, as the linewidth decreases, the capture velocity also decreases. Thus, the ability to capture relatively hot atoms from the atomic beam is decreased as the cooling laser photons are Doppler-shifted out of resonance for sufficiently hot atoms. Combining the best of both worlds, we employ a scheme where we first use

a blue MOT ($^1S_0 \rightarrow {}^1P_1$[32 MHz]) and then a red MOT ($^1S_0 \rightarrow {}^3P_1$[7.5 kHz]) to reduce the temperature of the atoms in the cloud further [38].

The transition $^1S_0 \rightarrow {}^3P_1$ is spin-forbidden and therefore the linewidth is much narrower than for the $^1S_0 \rightarrow {}^1P_1$ transition (see Figure 5.1). This results in a much lower Doppler limit for the red MOT (180 nK) than the blue MOT (768 µK). Thus, the Doppler limit and the recoil limit (230 nK) are very similiar for the red MOT.

First, the atoms are captured from the atomic beam using the blue MOT on the $^1S_0 \rightarrow {}^1P_1$ (461 nm) transition. Some atoms may decay into the long-lived $^3P_2$ state. A laser at 707 nm repumps those atoms to the ground state through the intermediate state $^3P_2 \rightarrow {}^3S_1 \rightarrow {}^3P_1 \rightarrow {}^1S_0$. In the process, atoms may also be pumped to the long-lived $^3P_0$ clock state. Those atoms are pumped back to the ground state by a second repump laser at 679 nm.

After approximately 1 s the atoms are transferred to the red MOT on the $^1S_0 \rightarrow {}^3P_1$ (689 nm) transition. The initial stage of the red MOT, light is frequency modulated with an amplitude of 1.5 MHz. This allows for the capture of atoms that are detuned from resonance due to their thermal Doppler shift. The amplitude of the frequency modulation is reduced as a function of time to efficiently cool atoms in the red MOT. Relatively high transfer efficiency of approximately 10 % is achieved using this technique. The transfer efficiency is mainly limited by the total available cooling laser power.

The magnetic moment of the ground state of strontium-87 is purely nuclear. Thus, the magnetic moment for the ground and $^3P_1$ states differ significantly [39]. This, combined with the narrow linewidth of the $^1S_0 \rightarrow {}^3P_1$ transition, results in some m_F states that are not trappable after being excited to the $^3P_1$ state. Thus, a single red MOT laser on the $^1S_0\,(m_F = 9/2) \rightarrow {}^3P_1\,(m_F = 11/2)$ transition is only able to cool a certain class of m_F states, so a second laser, red detuned from the $^1S_0\,(m_F = 9/2) \rightarrow {}^3P_1\,(m_F = 9/2)$ transition, is needed to remix or "stir" the m_F states so that every atom spends some time in a state that can be cooled [34].

The atoms are transferred from the red MOT to a crossed optical dipole trap, which is described in the next section.

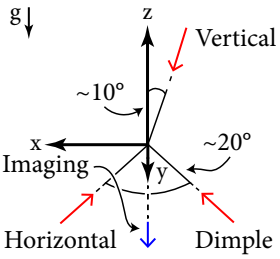

FIGURE 5.2: Optical dipole trap *k*-vectors (red) and imaging probe beam direction. Note that the angles are not to scale and only approximate values.

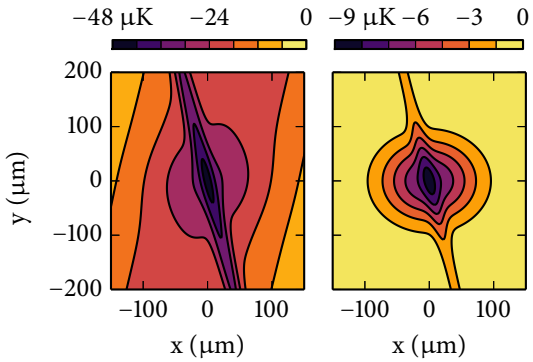

FIGURE 5.3: Optical dipole trap potential (U/k_B) in the x-y plane at $z = 0$ before (left) and after (right) evaporation. Features from all three laser beams are clearly visible in the left plot. See Figure 5.2 for definition of coordinates. All values are calculated using the beam $1/e^2$ radii and intensities.

5.3 CROSSED OPTICAL DIPOLE TRAP

We use three laser beams for our optical dipole trap. We start with a crossed dipole trap to capture atoms from the red MOT, and use a third, dimple, laser beam to improve evaporation.

Laser light from the 1064 nm laser setup, described in Section 3.2, is used to generate the optical dipole potential. All optical dipole laser beams are intensity stabilized using the methods described in Chapter 4.

The confinement of a single Gaussian beam dipole trap is different in the transverse and longitudinal direction (compare Section 2.2). Therefore, we use two beams (horizontal and vertical) to provide comparable confinement along both directions. The horizontal beam ($1/e^2$ radius of 240×40 µm) provides good spatial overlap with the red MOT and helps to maximize the transfer efficiency. The vertical beam ($1/e^2$ radius of 106 µm) provides confinement in the longitudinal direction of the horizontal beam. An additional beam, the dimple beam ($1/e^2$ radius of 17 µm), is used to provide very tight confinement for the coldest atoms. This helps to increase the efficiency of evaporation through faster thermalization. The k-vectors of the different beams are shown in Figure 5.2 and Figure 5.3 shows a cross-section of the optical dipole potential of all three beams.

The next section presents first results from evaporation in the optical dipole trap.

5.4 EVAPORATIVE COOLING

We use the optical dipole trap to evaporatively cool strontium atoms. This section first reports the results from evaporation and then discusses the methods. Note that the results presented in this section are preliminary.

We start evaporation with 5×10^5 atoms at 1 µK and a trap depth of approximately 30 µK. The temperature is reduced to 70 nK and the atom number to 2×10^4 as the trap

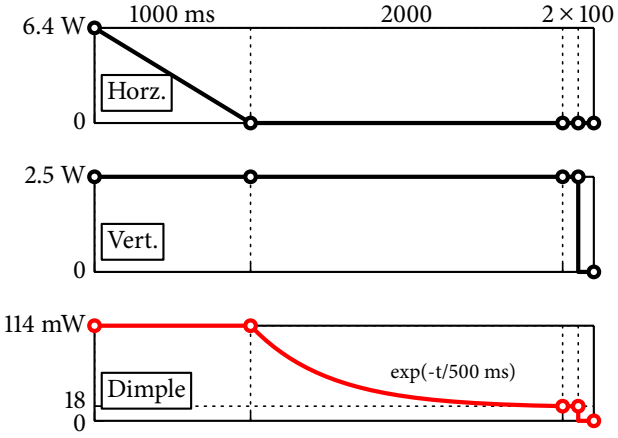

FIGURE 5.4: Experimental sequence for evaporative cooling. The change of the power in the three optical dipole trap beams is shown. All waveforms are linear/step ramps except for the evaporation, which follows an exponential interpolated with ten equispaced linear ramps. Note that the experimental sequence for the MOTs (before) and the imaging (after) is not shown.

depth is lowered to approximately 1.5 μK during evaporation. We reach a minimum of T/T_F of $\approx$ 0.5 per spin state assuming the population is a uniform mixture of ten spin states (the actual spin distribution is currently under investigation). If the nuclear spins are populated across only a few selected states, then T/T_F per spin state will be lower.

Evaporation in our experiment is done in two steps: We start with all three optical dipole beams at constant intensity. First, the horizontal beam is ramped down within one second. Second, we exponentially ($\exp(-t/500\,\text{ms})$) ramp down the dimple trap over two seconds while holding the vertical beam at constant intensity. See Figure 5.4 for the exact experimental sequence and beam powers. Note that the experimental sequence is not fully optimized yet.

Absorption imaging is used to estimate the number of atoms [40]. The probe beam is resonant with the blue transition ($^1S_0 \rightarrow {}^1P_1$). For the results in this thesis, the side imaging system with a resolution on the order of 10 μm was used. It allows us to track the atomic cloud in time of flight images. All images are triggered at the

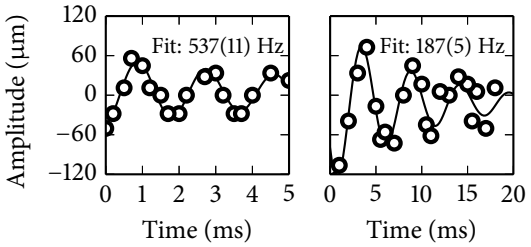

FIGURE 5.5: Measurement of trap frequencies in the dimple trap along z by observing the center of mass motion in time of flight images. The trap frequencies are shown before (left) and after evaporation (right). The data is fitted to an exponentially decaying sine. The signal-to-noise ratio for the data before the evaporation is better due to a higher number of atoms.

end of the evaporation sequence and analyzed by the Matlab program edcam[1]. This allows us to extract atom number, position, and the size of the atomic cloud. We fit the atomic cloud to a Gaussian, which is a valid approximation in the regime of operation (see Section 2.4) and calculate temperature by fitting to the atomic size as a function of time of flight. Figure 5.6 shows a time of flight image sequence and the temperature fit to a Gaussian distribution with

$$\sigma(t) = \sqrt{\sigma_0^2 + t^2 \frac{k_B T}{M}}. \tag{5.1}$$

Here, t is the time of light, $\sigma(t)$ is the size of the atomic cloud at time t, σ_0 the size of the atomic cloud (convolved with the point spread function of the imaging system) at $t = 0$, T the temperature of the atoms, and M the mass of a strontium-87 atom.

The trap frequencies are measured by increasing the dimple trap intensity momentarily (10 ms) and recording the position of the atomic cloud after turning the dimple dipole trap back on. The atoms are displaced from the center of mass due to gravity as the trap depth is increased. As soon as the trap is turned back on, the center of mass oscillates around the minimum of the harmonic potential at the trapping frequency. This allows us to see the oscillations of the center of mass. We can only measure the trapping frequency against gravity with this method. However, we assume a symmetric dimple beam. Thus, this method gives a lower bound on the transverse trapping frequency as the vertical optical dipole trap enhances the trapping frequency along one direction. We estimate the longitudinal trapping frequency to be 60 Hz, which is set by the properties of the two crossed beams. We measure a trapping frequency along z of 537 Hz at the beginning and 187 Hz at the end of the evaporation. This allows us to calculate the Fermi energy and Fermi temperature as described in Section 2.4.

For the results presented in this section, magnetic spin distributions were not measured. Thus the presented value for T/T_F is an upper bound for an equal distribution across all ten nuclear spin states of the ground state.

5.5 CONCLUSION AND OUTLOOK

The physics of optical trapping were explained and we derived rate equations for heating in optical dipole traps. We presented a high power laser system that is able to deliver up to approximately 20 W of 1064 nm light to the atoms via photonic crystal fibers and is stable as well as robust. This allows us to trap and evaporatively cool atoms in optical dipole traps. We built an intensity servo and photodetectors, which are used to suppress the intensity noise up to 40 dB. Finally, we presented first

[1] See `http://bitbucket.org/amoberkeley/edcam` for source code and details.

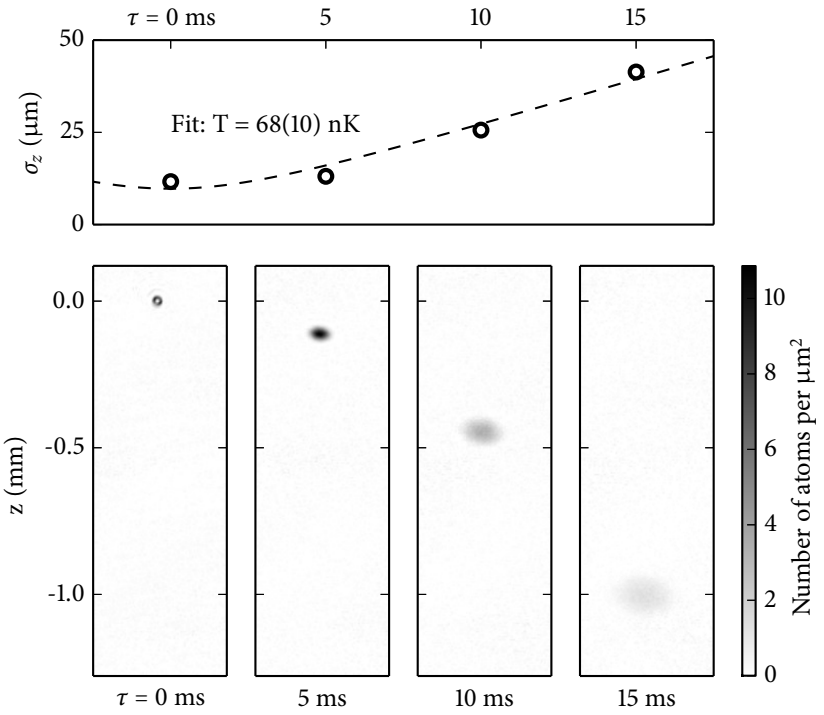

FIGURE 5.6: Temperature measurement after evaporation using time of flight images (bottom). Note that the images are averaged over four shots and the image at $\tau = 0$ ms is distorted/saturated due to high density of the atomic cloud. The plot (top) shows a fit to a Gaussian density distribution, which yields the value for the temperature. The statistical error bars are smaller than the datapoints and not shown in the plot.

experimental results from evaporative cooling in the optical dipole trap where we reach T/T_F of 0.5 per spin state, assuming equal distributions across all ten nuclear spin states.

As a next step, evaporative cooling has to be optimized to reach lower temperatures and larger number of atoms. Ref. [20] has demonstrated cooling of strontium-87 to $T/T_F = 0.1$ per spin state, which should be achievable in our setup as well. After finishing 813 nm laser setup, we should be able to load atoms into the lattice and optimize the transfer efficiency and lifetime in the lattice. The first completly new application of this experiment could be a clock measurement in a three-dimensional optical lattice and characterization of ac Stark shifts therein.

REFERENCES

[1] T. L. Nicholson et al. "Systematic evaluation of an atomic clock at 2×10^{-18} total uncertainty". In: *Nature Communications* 6 (Apr. 2015).

[2] M. J. Martin. "Quantum Metrology and Many-Body Physics: Pushing the Frontier of the Optical Lattice Clock". PhD thesis. JILA/CU Boulder, 2013.

[3] A. V. Gorshkov et al. "Two-orbital SU(N) magnetism with ultracold alkaline-earth atoms". In: *Nature Physics* 6.4 (Apr. 2010), pp. 289–295.

[4] G. A. Askar'yan. "Effects of the Gradient of a Strong Electromagnetic Beam on Electrons and Atoms". In: *J. Exptl. Theoret. Phys. (U.S.S.R)* 42.1567–1570 (Dec. 1962).

[5] R. Grimm, M. Weidemüller, and Y. B. Ovchinnikov. "Optical Dipole Traps for Neutral Atoms". In: *Advances In Atomic, Molecular, and Optical Physics*. Ed. by B. Bederson and H. Walther. Vol. 42. Academic Press, 2000, pp. 95–170.

[6] B. E. A. Saleh and M. C. Teich. *Fundamentals of Photonics*. 2nd ed. Wiley, 2007.

[7] T. A. Savard, K. M. O'Hara, and J. E. Thomas. "Laser-noise-induced heating in far-off resonance optical traps". In: *Physical Review A* 56.2 (1997), pp. 1095–1098.

[8] Miller and Childers. *Probability and random processes*. 1st ed. Academic Press, 2004.

[9] W. Ketterle and M. W. Zwierlein. "Making, probing and understanding ultracold Fermi gases". In: *ArXiv e-prints* (Jan. 2008). arXiv: `0801.2500 [cond-mat.other]`.

[10] T. J. Kane and R. L. Byer. "Monolithic, unidirectional single-mode Nd:YAG ring laser". In: *Opt. Lett.* 10.2 (Feb. 1985), pp. 65–67.

[11] M. Arrigoni, O. Haupt, and V. Leonhardt. *Ultra-Low Noise and Narrow Linewidth*. URL: `https://www.coherent.com/downloads/WP1_MephistoNPRO_Final.pdf` (visited on 11/17/2015).

[12] V. V. Ter-Mikirtychev. *Fundamentals of Fiber Lasers and Fiber Amplifiers*. Springer International, 2014.

[13] H. Pask et al. "Ytterbium-doped silica fiber lasers: versatile sources for the 1-1.2 mu;m region". In: *IEEE Journal of Selected Topics in Quantum Electronics* 1.1 (Apr. 1995), pp. 2–13.

[14] A. Kobyakov, M. Sauer, and D. Chowdhury. "Stimulated Brillouin scattering in optical fibers". In: *Adv. Opt. Photon.* 2.1 (Mar. 2010), pp. 1–59.

[15] R. G. Smith. "Optical Power Handling Capacity of Low Loss Optical Fibers as Determined by Stimulated Raman and Brillouin Scattering". In: *Appl. Opt.* 11.11 (Nov. 1972), pp. 2489–2494.

[16] NKT. *LMA-PM-15 Datasheet*. URL: http://www.nktphotonics.com/wp-content/uploads/2015/01/LMA-PM-15.pdf (visited on 11/20/2015).

[17] P. Russell. "Photonic Crystal Fibers". In: *Science* 299.5605 (2003), pp. 358–362.

[18] J. Knight et al. "Large mode area photonic crystal fibre". In: *Electronics Letters* 34 (June 1998), pp. 1347–1348.

[19] CVI/idex. *Material Properties*. URL: https://marketplace.idexop.com/store/SupportDocuments/MaterialProperties.pdf (visited on 11/19/2015).

[20] S. Stellmer, R. Grimm, and F. Schreck. "Production of quantum-degenerate strontium gases". In: *Phys. Rev. A* 87 (1 Jan. 2013).

[21] M-SQUARED. *SolsTis Datasheet*. URL: http://www.m2lasers.com/media/74139/solstis_datasheet_1014.pdf (visited on 11/20/2015).

[22] J. Pitman. *Probability*. Springer New York, 1993.

[23] P. J. Collings. "Simple measurement of the band gap in silicon and germanium". In: *Am. J. Phys* 48.3 (1980), pp. 197–199.

[24] T. Pearsall. "Ga0.47In0.53As: A ternary semiconductor for photodetector applications". In: *IEEE Journal of Quantum Electronics* 16.7 (July 1980), pp. 709–720.

[25] Hamamatsu. *G12180 Datasheet*. July 2015. URL: http://www.hamamatsu.com/resources/pdf/ssd/g12180_series_kird1121e.pdf (visited on 11/12/2015).

[26] Hamamatsu. *S3072 Datasheet*. Nov. 2014. URL: http://www.hamamatsu.com/resources/pdf/ssd/s3071_etc_kpin1044e.pdf (visited on 11/12/2015).

[27] B. V. Zeghbroek. *Principles of Semiconductor Devices - The p-n junction capacitance*. 2011. URL: http://ecee.colorado.edu/~bart/book/pncap.htm (visited on 11/11/2015).

[28] P. Horowitz and W. Hill. *The Art of Electronics*. 2nd ed. Cambridge University Press, 1989.

[29] P. C. D. Hobbs. *Building Electro-Optical Systems: Making it all Work*. 1st ed. Wiley, 2000.

[30] TI. *OPA843 Datasheet*. Dec. 2008. URL: http://www.ti.com/lit/ds/symlink/opa843.pdf (visited on 11/13/2015).

[31] R. Scott, C. Langrock, and B. Kolner. "High-dynamic-range laser amplitude and phase noise measurement techniques". In: *Selected Topics in Quantum Electronics, IEEE Journal of* 7.4 (July 2001), pp. 641–655.

[32] G. Franklin, J. D. Powell, and A. Emami-Naeini. *Feedback Control of Dynamic Systems*. 5th ed. Prentice Hall, 2005.

[33] S. W. Smith. *The Scientist & Engineer's Guide to Digital Signal Processing*. 1st ed. California Technical Pub, 1997.

[34] M. M. Boyd. "High precision spectroscopy of strontium in an optical lattice: Towards a new standard for frequency and time". PhD thesis. JILA/CU Boulder, 2007.

[35] M. M. Boyd et al. "Optical Atomic Coherence at the 1-Second Time Scale". In: *Science* 314.5804 (2006), pp. 1430–1433.

[36] D. J. Wineland and W. M. Itano. "Laser cooling of atoms". In: *Physical Review A* 20.4 (1979), pp. 1521–1540.

[37] Y. Castin, H. Wallis, and J. Dalibard. "Limit of Doppler cooling". In: *J. Opt. Soc. Am. B* 6.11 (1989), pp. 2046–2057.

[38] H. Katori et al. "Magneto-Optical Trapping and Cooling of Strontium Atoms down to the Photon Recoil Temperature". In: *Physical Review Letters* 82.6 (1999), pp. 1116–1119.

[39] S. Stellmer. "Degenerate quantum gases of strontium". PhD thesis. University of Innsbruck, 2013.

[40] T. Pyragius. "Developing and building an absorption imaging system for Ultracold Atoms". In: *ArXiv e-prints* (Sept. 2012). arXiv: 1209.3408 [physics.ins-det].

APPENDIX

I ELECTRONICS

A. TIA SCHEMATIC

Schematic of the TIA circuit. Note that C1, R1, and R2 need to be chosen accordingly to the capacitance of the photodiode D1 and the desired reverse bias.

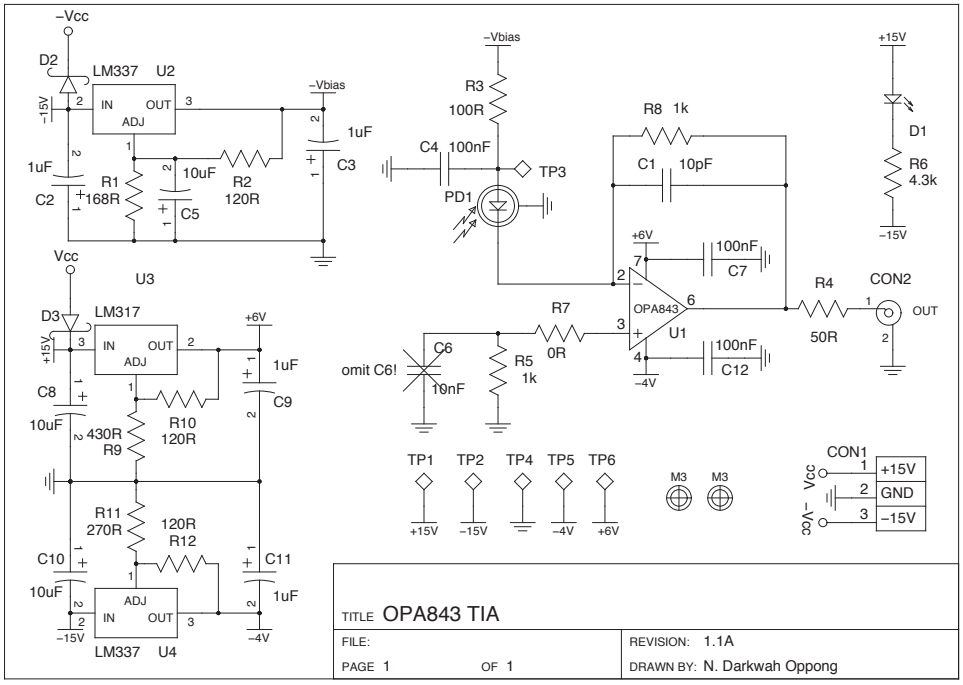

B. TIA PCB

Top and bottom layer of the PCB for the TIA. The silkscreen layer is shown in gray. Size of the PCB: 2000mil × 1500 mil (not shown to scale).

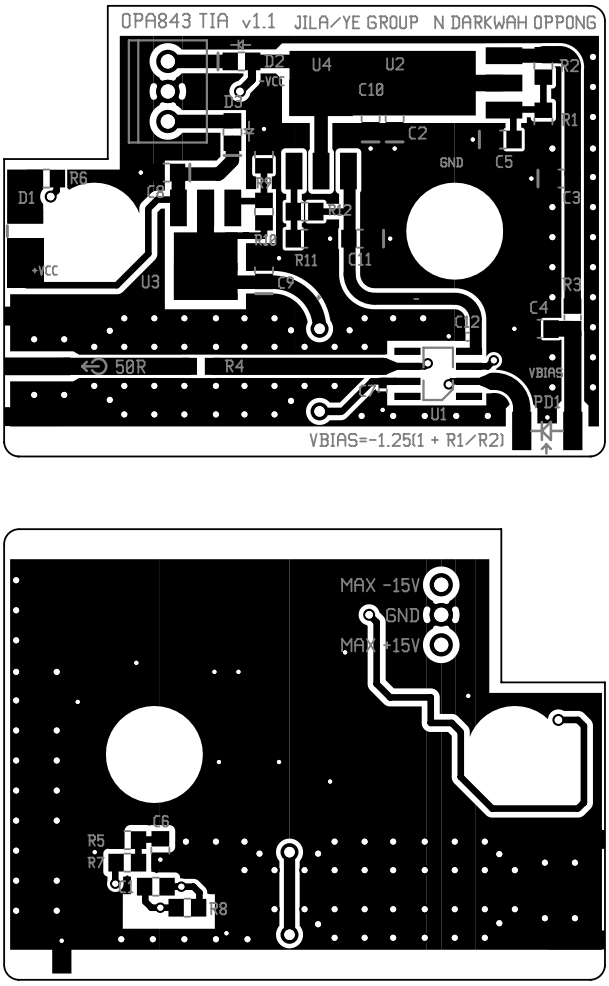

II SOURCE CODE

A. DIGITAL PID CONTROLLER

Python class for the digital PID controller described in Section 4.2.

```
from collections import deque

class PID:
    def __init__(self, current_value=0., setpoint=0., sampling_interval=1.,
         overall_gain=1., prop_gain=1., int_gain=1., diff_gain=0., min_max=(float('-
         inf'),float('inf')), offset=0):
        self.rbuffer = deque([0., 0.], maxlen=2)

        self.current_value = current_value
        self.setpoint = setpoint

        self.overall_gain = overall_gain
        self.min_max = min_max
        self.offset = offset

        self.sampling_interval = 0.
        self.prop_gain = 0.
        self.int_gain = 0.
        self.diff_gain = 0.

        self.error = 0.

        self.set_params(sampling_interval=sampling_interval,
                        prop_gain=prop_gain,
                        int_gain=int_gain,
                        diff_gain=diff_gain)

    def set_params(self, sampling_interval=False, overall_gain=False, prop_gain=False
         , int_gain=False, diff_gain=False):
        self.sampling_interval = sampling_interval or self.sampling_interval
        self.prop_gain = prop_gain or self.prop_gain
        self.int_gain = int_gain or self.int_gain
        self.diff_gain = diff_gain or self.diff_gain
        self.overall_gain = overall_gain or self.overall_gain

        self.update_filter_coefficients()

    def update_filter_coefficients(self):
        G = self.overall_gain
        T = self.sampling_interval
        p = G*self.prop_gain
        i = G*self.int_gain
        d = G*self.diff_gain

        self.filter_coefficients = {
            'b_0': p + i*T/2. + d*2./T,
            'b_1': i*T - d*4./T,
            'b_2': i*T/2. - p + d*2./T,
            'a_1': 0.,
            'a_2': -1.
        }

    def tick(self, current_value=None):
        if current_value != None:
```

```
52              self.current_value = current_value
53
54          self.error = self.current_value - self.setpoint
55
56          a_1 = self.filter_coefficients['a_1']
57          a_2 = self.filter_coefficients['a_2']
58          b_0 = self.filter_coefficients['b_0']
59          b_1 = self.filter_coefficients['b_1']
60          b_2 = self.filter_coefficients['b_2']
61
62          w = self.rbuffer
63          x = self.error
64
65          # bilinear transform of continous PID transfer function
66          v = x - a_1*w[-1] - a_2*w[-2]
67          y = b_0*v + b_1*w[-1] + b_2*w[-2]
68          w.append(v)
69
70          # offset
71          y += self.offset
72
73          # clamp
74          if y < self.min_max[0]: y = self.min_max[0]
75          if y > self.min_max[1]: y = self.min_max[1]
76
77          self.output = y
78
79          return y
80
81      def reset(self):
82          for i, e in enumerate(self.rbuffer): self.rbuffer[i] = 0.
83
84          self.current_value = 0.
85          self.output = 0.
```

The complete source code for the GUI and the laser network interface can be found at `https://github.com/yesrgang/m2-frequency-servo`.